

1                    **Aquatic Biogeochemical Eddy Covariance Fluxes in the Presence of Waves**

2

3 **Matthew H. Long<sup>1</sup>**

4

5 <sup>1</sup>Marine Chemistry and Geochemistry Department, Woods Hole Oceanographic Institution, 266  
6 Woods Hole Road, MS#8, Woods Hole, Massachusetts, USA, 02543

7

8 corresponding author: Matthew Long ([mlong@whoi.edu](mailto:mlong@whoi.edu))

9

10 **Key Points:**

- 11            • Literature review of eddy covariance studies reveals a majority of studies were conducted  
12            in shallow waters where waves bias measurements
- 13            • Sampling higher above the boundary shifts turbulence to longer scales, producing a spectral  
14            gap between wave and turbulent frequencies
- 15            • Paradigm shift in how studies are conducted and analyzed will enable the removal of wave  
16            bias and new chemical tracer applications

17 **Abstract**

18         The eddy covariance (EC) technique is a powerful tool for measuring atmospheric  
19 exchange rates that was recently adapted by biogeochemists to measure aquatic oxygen fluxes. A  
20 review of aquatic biogeochemical EC literature revealed that the majority of studies were  
21 conducted in shallow waters where waves were present, and that waves biased sensor and  
22 turbulence measurements. This review identified that larger measurement heights shifted  
23 turbulence to lower frequencies, producing a spectral gap between turbulence and wave  
24 frequencies. However, most studies sampled too close to the boundary to allow for a spectral  
25 turbulence-wave gap, and will require a paradigm shift in how EC measurements are conducted to  
26 remove wave-bias. EC fluxes have only been derived from the time-averaged product of vertical  
27 velocity and oxygen, often resulting in wave-biased fluxes. Presented here is a new analysis  
28 framework for removing wave-bias by accumulation of cross-power spectral densities below wave  
29 frequencies. This analysis framework also includes new measurement guidelines based on wave  
30 period, currents, and measurement heights. This framework is applied to sand, seagrass, and reef  
31 environments where traditional EC analysis resulted in wave-bias of  $7.2 \pm 5.8\%$  error in  
32 biogeochemical (oxygen and  $H^+$ ) fluxes, while more variable and higher error was evident in  
33 momentum fluxes ( $10.4 \pm 20.5\%$  error). It is anticipated that this framework will lead to significant  
34 changes in how EC measurements are conducted and evaluated, and help overcome the major  
35 limitations caused by wave-sensitive and slow-response sensors, potentially expanding new  
36 chemical tracer applications and more widespread use of the EC technique.

37

38 **Plain Language Summary**

39         The exchange of vital nutrients between the seafloor, overlying water, and the atmosphere  
40 is paramount to our understanding of the global cycling of these substances. Techniques that  
41 measure water transport and nutrients have revolutionized how these exchanges are studied, and  
42 how they impact local water quality, productivity, and nutrient cycling. Through measurements of  
43 the nutrient content of water, and their transport by water movement, the exchange of nutrients can  
44 be determined. These techniques were originally developed to examine exchange between the land  
45 and atmosphere, but applying these techniques to aquatic ecosystems has presented challenges due  
46 to surface waves that are present in the shallow aquatic ecosystems where these aquatic techniques  
47 are commonly applied. Waves cause errors in the sensors used to measure water transport and  
48 nutrients, and have presented significant challenges for applying these atmospheric techniques  
49 underwater. This research presents new guidelines for these aquatic exchange measurements that  
50 will require a paradigm shift in how measurements are conducted and analyzed, to allow for  
51 nutrient exchange measurements in the presence of waves. These new guidelines also allow for  
52 new sensors that were previously incompatible, expanding the applications of these techniques to  
53 new scientific research questions.

54

## 55 **1 Introduction**

56 Eddy covariance and related boundary layer exchange techniques have been used in  
 57 terrestrial ecosystems since the early 1950s to measure fluxes of water and heat (Swinbank 1951)  
 58 and are widely applied today to measure a variety of biogeochemical and energy fluxes in the  
 59 atmospheric boundary layer (e.g. Baldocchi 2003, Lee et al. 2004, Burba and Anderson 2010). The  
 60 physical oceanography community has applied this atmospheric boundary layer theory to fluxes  
 61 of momentum, heat, and salt in marine settings, where waves have been identified as a unique  
 62 source of bias in oceanic turbulence measurements (Trowbridge 1998, Scully et al. 2016,  
 63 Trowbridge et al. 2018). The application of boundary layer theory to aquatic biogeochemical  
 64 fluxes is comparatively new, and has mainly been used to examine oxygen (O<sub>2</sub>) fluxes as a proxy  
 65 for carbon exchange.

66 The aquatic eddy covariance (EC) technique measures the flux of solutes between the  
 67 benthic surface and the overlying water (Berg et al. 2003, Lorrai et al. 2010, Reimers et al. 2012).  
 68 EC measurements are widely considered the most reliable flux method because they require the  
 69 fewest physical assumptions (Fairall et al. 2000). The aquatic EC technique has been used in  
 70 challenging environments, where traditional methods are difficult to apply, such as benthic  
 71 macrophytes (Hume et al. 2011, Koopmans et al. 2020), sea-ice (Long et al. 2012a, Glud et al.  
 72 2014), lakes (Brand et al. 2008, McGinnis et al. 2008), rocky substrates (Glud et al. 2010, Attard  
 73 et al. 2019), oyster beds (Reidenbach et al. 2013, Volaric et al. 2018), the deep sea (Berg et al.  
 74 2009, Donis et al. 2016), and coral reefs (Long et al. 2013; 2019, Rovelli et al. 2015) and represents  
 75 a highly-advantageous methodology for examining high temporal resolution, ecosystem-level  
 76 fluxes in complex environments. The aquatic EC technique has been occasionally applied to other  
 77 tracers including temperature (Crusius et al. 2008, Long et al. 2012a, Else et al. 2015), salinity  
 78 (Crusius et al. 2008), nitrate (Johnson et al. 2011), hydrogen sulfide (McGinnis et al. 2011) and  
 79 pH (Long et al. 2015a). The aquatic EC technique has also been applied to the atmosphere-water  
 80 interface to measure atmospheric O<sub>2</sub> exchange (Berg and Pace 2017; Long and Nicholson 2018)  
 81 and at the oxycline and thermoclines in lakes (Kreling et al. 2014, Weck and Lorke 2017).

82 The basis for the EC technique is that turbulent mixing, caused by the interaction of current  
 83 velocity with the benthic, atmospheric, sea-ice, or cline interfaces, is the dominant vertical  
 84 transport process in boundary layers. Therefore, vertical fluxes across the ecosystem interfaces can  
 85 be derived from high temporal resolution measurements of the vertical velocity and a solute  
 86 concentration. The time-averaged EC flux across an interface are determined by:

$$87 \quad Flux = \overline{w'c'} \quad Eq. 1$$

88 where the overbar represents a time average, and  $w'$  and  $c'$  are the fluctuating components of the  
 89 vertical velocity and scalar concentration ( $c$ ), respectively, that are measured at the same point at  
 90 a fixed distance away from the interface.

91 Recent work has highlighted the influence of wave and current variability on EC  
 92 measurements (Donis et al. 2015, Holtappels et al. 2015, Berg et al. 2015, Reimers et al. 2016a)  
 93 when applying the most commonly used sensor in aquatic EC measurements, the Clark-type O<sub>2</sub>  
 94 microsensor (Revsbech 1989). Studies demonstrating wave bias have indicated that automated  
 95 numerical time-lag corrections (for slow or spatially separated sensors) can be biased by wave  
 96 orbital motion (Berg et al. 2015, Donis et al. 2015), that cospectral analysis reveals significant  
 97 contributions to fluxes at wave frequencies (Kuwae et al. 2006, Long et al. 2015b, Reimers et al.  
 98 2016a), and that Clark-type oxygen sensors can be biased by zero-crossing wave velocities

99 (Holtappels et al. 2015, Reimers et al. 2016a). These Clark-type microsensors have been designed  
 100 to limit “stirring sensitivity” by reducing the tip size and microsensor design, but trade-offs exist  
 101 between maximizing response time and reducing stirring sensitivity (Revsbech 1989). In  
 102 comparison, optical O<sub>2</sub> sensors (i.e. optodes) have been applied more frequently since their  
 103 introduction to aquatic EC (Chipman et al. 2012) because they have the advantage of not  
 104 consuming O<sub>2</sub>, making them less susceptible to stirring sensitivity as there is no net transport of  
 105 O<sub>2</sub> to the sensor (Klimant et al. 1995). However, recent work has also suggested that optodes, like  
 106 commonly used Clark-type sensors, may have a variable response time due to changes in the  
 107 boundary layer thickness caused by wave motions or zero-crossing velocities that temporarily limit  
 108 transport to the sensor, an effect that peaks at the frequency of the waves (Berg et al. 2015, Reimers  
 109 et al. 2016a). To prevent sensor bias, microfluidic sensor housings (pumping fluid from the  
 110 measurement point to negate wave velocities) and rotating instrument designs (preventing biased  
 111 sensor separation corrections due to waves or orthogonal currents) have been developed, but also  
 112 complicate instrument engineering (Long et al. 2015a, Long et al. 2019).

113 The issue of waves, which is unique to aquatic EC, has largely focused on the  
 114 biogeochemical sensors, but wave bias in the turbulence measurements from acoustic sensors is  
 115 also of major concern (Trowbridge 1998, Shaw and Trowbridge 2001, Scully et al. 2016). Wave-  
 116 bias in the turbulent velocities used to calculate fluxes have been observed due to slight variations  
 117 in instrument orientation, leading to some of the horizontal wave-associated velocities  
 118 contaminating the vertical velocity (Trowbridge 1998, Long et al. 2015b, Reimers et al. 2016a,  
 119 Scully et al. 2016, Trowbridge et al. 2018). This contamination of vertical velocity by waves is a  
 120 problem when turbulence and surface waves are observed at similar or overlapping frequencies  
 121 (Trowbridge 1998, Scully et al. 2016, Long and Nicholson 2018). However, a careful  
 122 consideration of site hydrodynamic conditions and instrument configurations can enable a process  
 123 to ensure the wave and turbulence frequencies do not overlap, thereby allowing for the spectral  
 124 separation of turbulence and waves (Scully et al. 2016, Long and Nicholson 2018), effectively  
 125 removing any effect that high-frequency surface waves have on chemical sensor or turbulence  
 126 measurements.

127 Scully et al. (2016) describes and applies a procedure for removing wave bias in turbulence  
 128 measurements in coastal settings, based on the frequency differences between turbulence and wave  
 129 period ( $T_d$ ). The Taylor frozen turbulence hypothesis relates wavenumber ( $k$ ) to frequency ( $f$ ) based  
 130 on the mean advection speed ( $U$ ), as:

$$131 \quad k = \frac{2\pi f}{U} \quad \text{Eq. 2}$$

132 Both atmospheric and oceanic measurements of momentum cospectra suggest that under  
 133 unstratified conditions, the peak of the variance preserving cospectra occurs at  $k \sim 1/z$ , where  $z$  is  
 134 the height above the bottom where measurements are conducted (Wyngaard and Cote, 1972; Gerbi  
 135 et al., 2008). Therefore, as long as the frequencies associated with the dominant surface waves  
 136 ( $1/T_d$ ) are high and the mean advection speed is low, all of the turbulent fluctuations will be at  
 137 frequencies lower than the surface waves when:

$$138 \quad \frac{2\pi z}{UT_d} > 1 \quad \text{Eq. 3.}$$

139 For example, at common shallow water conditions where the values of  $T_d$  do not exceed 4 seconds  
 140 and tidal currents are  $< 0.2 \text{ m s}^{-1}$ , this relationship is easily satisfied if measurements are conducted  
 141 at  $z = 0.4 \text{ m}$  away from the benthic surface (i.e.  $[(2\pi z)/(UT_d) = 3.1]$ ), whereas a measurement height

142 at  $z = 0.1$  m away from the benthic surface would not (i.e.  $[(2\pi z)/(UT_d) = 0.8]$ ). This method has  
143 been used to calculate turbulent fluxes by filtering out frequencies at and above the wave  
144 frequencies and has demonstrated that there is typically a clear spectral gap between the frequency  
145 of the dominant surface waves and the dominant frequencies of the turbulent flux when  
146 measurements are conducted at sufficient heights away from the interface boundary (Scully et al.  
147 2016).

148 This manuscript addresses a major issue that limits the application of boundary layer  
149 exchange techniques, specifically the aquatic eddy covariance technique, in shallow environments  
150 where waves are present. A primary objective of this highly interdisciplinary topic is to produce  
151 and communicate results that are easily discernable and translatable to the aquatic EC community.  
152 A review of existing aquatic EC literature is presented to highlight the predominance of EC  
153 applications in shallow water where waves are likely to be present, and the conditions and  
154 configurations of previous EC studies. A new analysis framework for flux calculation is presented,  
155 where the cross-power spectral density is accumulated from low frequencies, up to the wave  
156 frequencies, to calculate interface fluxes. This method effectively removes wave bias from both  
157 sensor and turbulence measurements, and specific guidelines are provided to ensure that this  
158 method can be applied, based on site hydrodynamics and instrument configurations. Also  
159 presented is the potential use of slow-response sensors using these same guidelines that will enable  
160 a wider range of sensors to be applied to the EC technique in the future.

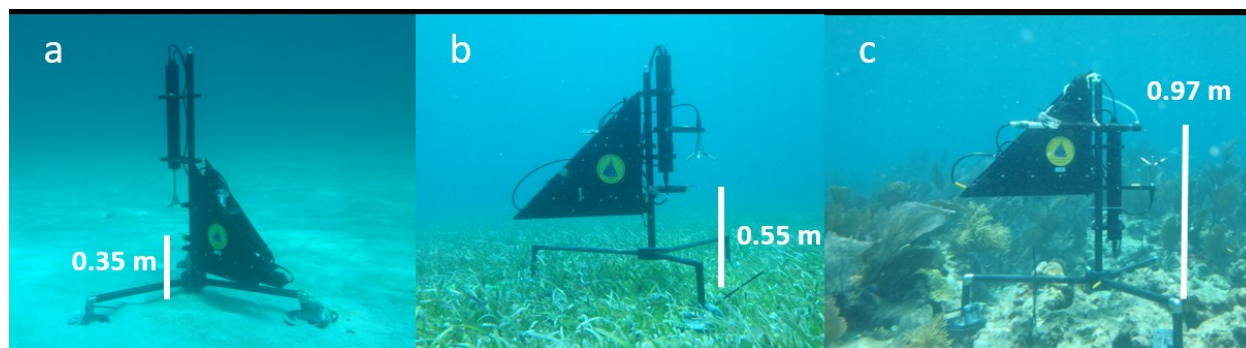
161

## 162 **2 Methods**

163 *2.1 Literature Review* – This research presents a review of the EC literature consisting of 62 field-  
164 based manuscripts published since the introduction of aquatic oxygen EC for biogeochemical  
165 investigations (Berg et al. 2003). These manuscripts were separated to different study sites defined  
166 by either, having different measurement heights or, different water depths. In manuscripts where  
167 a range of sites with different depths were analyzed, the smallest and greatest depths are reported.  
168 The depths, measurement heights, solutes, sensors, benthic roughness elements, environment,  
169 burst length, and Reynolds decomposition method were extracted from manuscript text when  
170 reported. Cospectral frequencies and peak current velocities were taken directly from the text or  
171 visually estimated from figures. Measurement heights of the sensors were modified by subtracting  
172 biological canopy heights or physical barrier heights when reported.

173 *2.2 Field Sites* – The field sites were located ~7 km offshore of Key Largo, Florida, USA at the  
174 southern tip of Florida in the Florida Keys. The sites were located on or adjacent to Little Grecian  
175 Rocks Reef with a site on the reef crest (25.119016°N, -80.300504°W, Figure 1c) at 2.9 m mean  
176 depth, in a seagrass bed located ~225 m to the northwest of the reef site (25.120328°N, -  
177 80.302222°W, Figure 1b) at 4.8 m mean depth, and in a sandy site located ~300 m to the southwest  
178 of the reef site (25.117320°N, -80.303069°W, Figure 1a) at 6.3 m mean depth. The reef site is  
179 described in substantial detail (3-dimensional and species analyses) in Hopkinson et al. (2020),  
180 where the EC instrument can be seen near the center of the image analyses (in Figure 6 of  
181 Hopkinson et al. 2020) during its deployment in this study. This reef site is substantially degraded  
182 with its benthic surface and primary production dominated by octocorals, algae and rubble  
183 (Hopkinson et al. 2020, Owen et al. 2020). The seagrass site was dominated by dense *Thalassia*  
184 *testudinum* (turtlegrass) with a canopy height of 0.2 m underlain by carbonate sands. The sandy  
185 site was composed of carbonate sands with microalgal mats (Figure 1a) and migrating bedforms

186 0.1 m in height. Research was conducted from June 24 to June 29 in 2018 with the seagrass  
187 deployment beginning on the 24th and the sand and reef deployment beginning on the 25th of  
188 June, 2018.



189  
190 Figure 1. Eddy Covariance Hydrogen ion and Oxygen Exchange Systems (ECHOES) deployed at  
191 sand (a), seagrass (b) and reef (c) sites on or adjacent to Little Grecian Rocks Reef in the Florida  
192 Keys, Florida, USA. Measurement heights are indicated by white bars and text.

193 *2.3 Instrumentation* – The EC systems used here, known as Eddy Covariance Hydrogen Ion and  
194 Oxygen Exchanged System (ECHOES, Long et al. 2015a) consisted of an Acoustic Doppler  
195 Velocimeter (ADV, Nortek) that was coupled to a FirestingO<sub>2</sub> Mini fiber-optic O<sub>2</sub> meter with a  
196 fast-response (~ 0.3 s) 430 μm diameter optode (Pyrosience) (Long et al. 2015a, Long and  
197 Nicholson 2018, Long et al. 2019) and a fast-response (~0.6 s, Figure S1) Honeywell Durafet® III  
198 pH sensor with a preamp Cap Adapter and a custom isolation amplifier (based on Texas  
199 Instruments ISO124P). The ECHOES systems logged the three-dimensional velocity, depth, O<sub>2</sub>  
200 optode, pH sensor, and triaxial Inertial Measurement Unit (IMU, MicroStrain model 3DM-GX3)  
201 at a frequency of 16 Hz continuously. Using 6 rechargeable lithium ion batteries (50 Watt h, Nortek  
202 #220007) the system could operate continuously for ~4.5 days. All instrumentation was mounted  
203 to a light-weight, passively rotating carbon fiber frame (Figure 1). A bubble level affixed to the  
204 ADV mount allowed for precise leveling during field deployment by SCUBA divers. Stakes (sand  
205 and seagrass sites) or lead weights and zip ties (reef site) maintained instrument location and  
206 orientation. The measurement height, or location of the ADV measuring volume and sensors,  
207 above the sediment surface was determined by placing it at a height that was greater than twice  
208 the canopy or bedform height (Figure 1) as recommended by terrestrial EC guidelines where twice  
209 the canopy height, and up to 5 times the canopy height in patchy environments, is recommended  
210 (Burba and Anderson 2010, Long et al. 2015b).

211 The microfluidic flow-through sensor design has a small volume (0.33 cm<sup>3</sup>) and a KNF  
212 Micropump (model NF10) with a flow rate (100 mL min<sup>-1</sup>) that combine to have a quick flush rate  
213 (5 Hz) while protecting and preventing light interference for both O<sub>2</sub> and pH sensors. The  
214 microfluidic intake was located 0.025 m behind the ADV measuring volume (see Donis et al. 2015,  
215 Berg et al. 2015) to prevent disruption of ADV-measured flow rates (Long et al. 2015a). The  
216 microfluidic housing mounted tightly over the Durafet III sensor tip and has a small chamber for  
217 inserting the O<sub>2</sub> optode, that is located at the end of a 0.04 m long, 0.003 m inside diameter copper  
218 intake tube and filter, with the outlet of the microfluidic chamber connected to the pump intake  
219 (Figure S2). A passive flow meter (0-100 ml min<sup>-1</sup>) connected to the pump outlet was used to  
220 confirm pumping rates during deployment.

221 A separate frame at each site contained an Odyssey (Dataflow Systems, New Zealand)

222 photosynthetically active radiation (PAR) sensor and a Seabird SeapHOx (measuring salinity,  
 223 temperature, depth, O<sub>2</sub>, and pH). The SeapHOx was factory calibrated and the Odyssey PAR  
 224 sensors were calibrated to a HR-4 spectroradiometer system (HOBI Labs HydroRAD-4) using the  
 225 methods of Long et al. (2012b).

226 *2.4 Eddy Covariance Analysis Framework* – The 16 Hz data were averaged to 8 Hz for analysis.  
 227 The ECHOES O<sub>2</sub> and pH sensors were calibrated to the slow-response SeapHOx sensors by least-  
 228 squares regression. The pH was converted to H<sup>+</sup> ion concentration for all calculations. The ADV  
 229 velocity data was removed from analysis when the beam correlation was < 50%. The means for  
 230 Reynolds decomposition were determined using a 5 minute moving average window. The period  
 231 over which the flux was determined, or burst length, was 15 minutes, with subsequent averaging  
 232 to hourly rates. Rotations were conducted automatically by Nortek software (Vector v1.39.09) to  
 233 East, North, and Up coordinates based on the IMU data (see Long and Nicholson 2018) followed  
 234 by a planar rotation (see Lorke et al. 2013) for each instrument deployment. Standard eddy  
 235 covariance analysis was conducted to calculate O<sub>2</sub>  $\overline{(w'O_2')}$ , H<sup>+</sup>  $\overline{(w'H^+)}$ , and momentum  
 236  $\overline{((w'u')^2 + (w'v')^2)}^{1/2}$  fluxes (e.g. Eq. 1) where  $u$  and  $v$  indicate the horizontal components of  
 237 the velocity and  $w$  represents the vertical velocity. Cross Power Spectral Densities were also used  
 238 to calculate O<sub>2</sub>, H<sup>+</sup> and momentum fluxes and were determined with the Matlab function “CPSD”,  
 239 with the removal of wave frequencies conducted by accumulating the CPSD at frequencies below  
 240 approximately  $1/(2T_d)$ . A storage correction was applied to all biogeochemical fluxes due to the  
 241 presence of biological canopies and the high measurement heights used (Lorrai et al. 2010,  
 242 Rheuban et al 2014a, Long and Nicholson 2018). Power spectral densities were determined using  
 243 the Matlab function “PWELCH”. The  $T_d$  was determined by finding the maximum of the  
 244 momentum CPSD at the frequencies where the waves were expected for the study sites (e.g.  $0.1 >$   
 245  $\text{Hz} < 1$ ). Wave velocities were estimated by:

$$246 \quad \text{wave velocity} = \left( \overline{(u' - \bar{u})^2} + \overline{(v' - \bar{v})^2} + \overline{(w' - \bar{w})^2} \right)^{1/2} \quad \text{Eq. 4}$$

247 where the prime indicates the instantaneous velocity and the overbars indicate averaging over each  
 248 burst. Flux methods were compared by linear regression. The normalized root square error  
 249 (NRSME) was determined by calculating the square root of the square of the difference between  
 250 flux methods, averaging this value across each deployment and scalar, and normalizing this to  
 251 percent by dividing by the range of the flux. This normalization method was used as the net, or  
 252 average of the biogeochemical fluxes, is close to zero and would result in erroneous results.

253

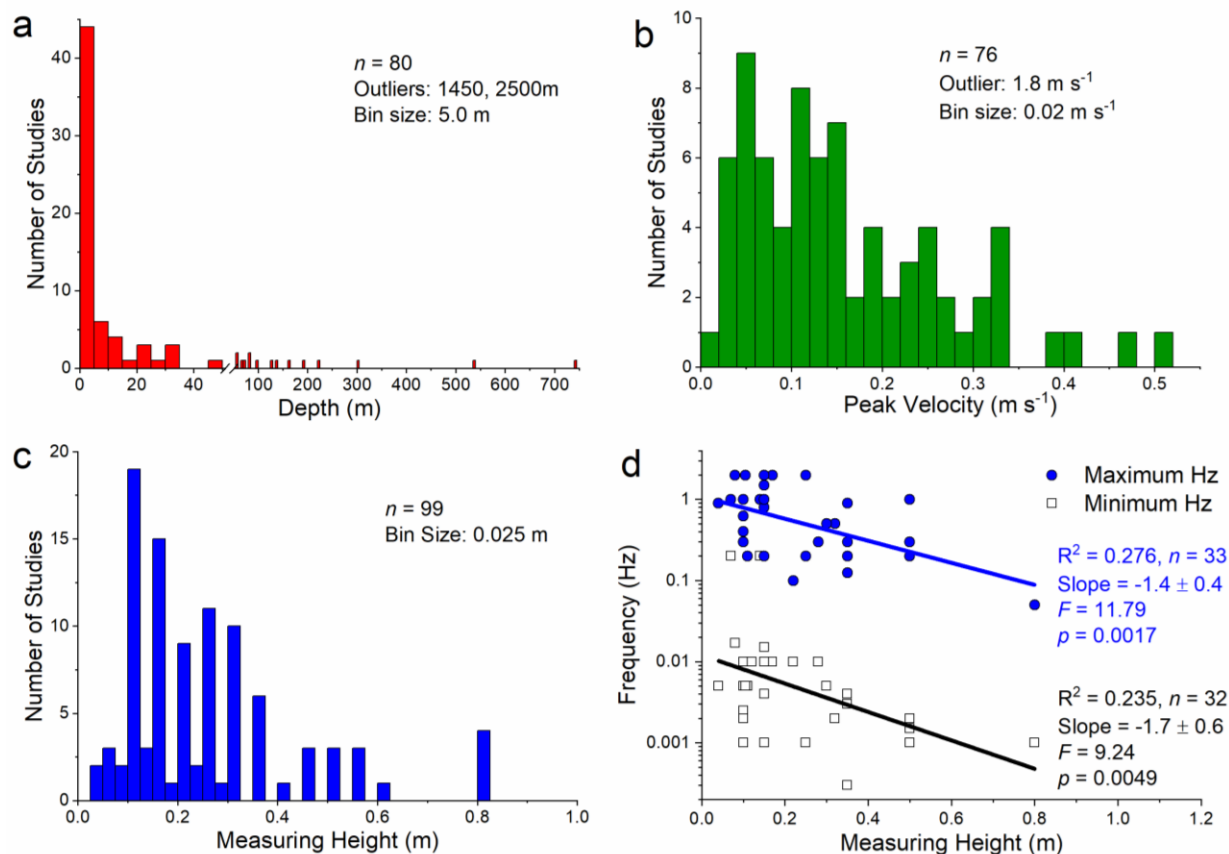
### 254 **3 Results**

255 *3.1 Literature Review* - A total of 62 aquatic field-based biogeochemical EC manuscripts were  
 256 identified (see Supplemental Information), which, when separated to individual studies based on  
 257 different water depths and measurement heights, resulted in 102 studies for the purposes of this  
 258 analysis (excluding this study). The use of Clark-type O<sub>2</sub> microsensors dominated ( $n = 80$  studies,  
 259 starting from Berg et al. 2003) with O<sub>2</sub> optodes becoming more popular recently ( $n = 20$ , starting  
 260 from Chipman et al. 2012). Other sensors applied to EC included temperature ( $n = 5$ ), galvanic O<sub>2</sub>  
 261 ( $n = 2$ ), conductivity ( $n = 1$ ), nitrate ( $n = 1$ ), hydrogen sulfide ( $n = 1$ ), and pH ( $n = 1$ ).

262 Previous studies have deployed the EC technique at water depths ranging from 0.3 to 2500  
 263 m, but the majority of these studies were conducted at depths of less than 5 m ( $n = 44$ , out of 80

264 studies reporting depth, Figure 2a). The mean peak current velocity of previous studies was  $0.175$   
 265  $\pm 0.219 \text{ m s}^{-1}$ , with a median of  $0.123 \text{ m s}^{-1}$ , and a range of  $0.015$  to  $1.8 \text{ m s}^{-1}$  (Figure 2b). The  
 266 mean measurement height of previous studies was  $0.25 \pm 0.17 \text{ m}$ , with a median of  $0.20 \text{ m}$ , and a  
 267 range of  $0.04$  to  $0.80 \text{ m}$  (Figure 2c). The majority of studies ( $n = 68$ , out of 99 studies reporting  
 268 measurement heights) used measurement heights of less than  $0.25 \text{ m}$  above the bottom. Some  
 269 studies reported physical or biological canopy roughness elements ( $n = 22$ ), which were subtracted  
 270 from the reported measurement heights, resulting in a corrected mean measurement height of  $0.206$   
 271  $\pm 0.178 \text{ m}$ , a median of  $0.15 \text{ m}$ , and a range of  $-0.365$  to  $0.8 \text{ m}$ .

272



273

274 Figure 2. Histograms of the depth of biogeochemical eddy covariance studies (a) and the peak  
 275 velocity measured in studies (b). Note the dominance of shallow-water studies where waves are  
 276 likely present. Histograms of measurement heights (uncorrected for canopy or physical barrier  
 277 heights) used in eddy covariance studies (c) and the associated frequencies of flux-carrying eddies  
 278 which shift to longer scales with increasing measurement heights (d) where statistics represent a  
 279 significant difference from a zero-slope line.

280 A total of 33 studies reported the contributing turbulent frequencies of the fluxes, which  
 281 displayed a decrease in frequency with increased measurement height (Figure 2d). Both the highest  
 282 and lowest contributing frequencies show a negative slope with increasing measurement height,  
 283 and a significant difference from a zero-slope line. Applying Eq. 3 to all previous studies indicated  
 284 that the mean of the conditions and instrument configurations may allow for the separation of  
 285 turbulence and wave frequencies (Table 1). However, the majority of studies ( $n = 68$ ) were

286 conducted at measurement heights  $< 0.25$  m and these low measurement heights combined with  
 287 mean study conditions suggest that a distinct separation between turbulent and wave frequencies  
 288 may not have been possible (Table 1).

Table 1. Demonstration of the potential for a spectral gap between turbulence and wave frequencies in different studies  
 Mean Measurement Height ( $z$ ) Peak Velocity ( $U$ ) Wave Period ( $T_d$ ) Eq 3:  $(2\pi z)/(UT_d)$

Site	m	$\text{m s}^{-1}$	s	
Previous studies ( $< 0.25\text{m}$ )	0.12 (-0.365 to 0.24 m, $n = 68$ )	0.172	*4.0	1.08
All previous studies	0.21 (-0.365 to 0.8 m, $n = 99$ )	0.175	*4.0	1.86
This study - Sand	0.35 (0.1m bedforms)	0.18	3.9	3.13
This Study - Grass	0.55 (0.2m canopy)	0.12	4.1	3.19
This Study - Reef	0.97 (0.5m canopy)	0.11	3.7	7.25

The \* indicates assumed values as the majority of studies ( $n = 94$ ) did not report wave period. When biological canopy or physical barrier heights are reported, these have been subtracted from the reported measuring heights (see Supplemental Information).

Numbers in parenthesis are the range and  $n$  from previous studies, or canopy and bedform heights (this study).

289  
 290 For conducting Reynolds decomposition, 33 manuscripts used linear detrending, 15 used a  
 291 moving or running average window, 7 used a combination or other method, and 7 did not report a  
 292 mean determination method. The burst length, or period over which fluxes are calculated, was  
 293 most commonly 15 min ( $n = 43$  manuscripts) followed by  $< 10$  minutes ( $n = 5$ ), 10 min ( $n = 4$ ), 30  
 294 min ( $n = 3$ ), 20 min ( $n = 1$ ), variable ( $n = 1$ ) or not reported ( $n = 5$ ). A range of different data and  
 295 time-series corrections including; velocity de-spiking (e.g. Goring and Nikora 2002), various  
 296 coordinate rotations (Reimers et al. 2012, Lorke et al. 2013), sensor time-lag corrections (Donis et  
 297 al. 2015, Berg et al. 2015), low frequency wave corrections (Reimers et al. 2016b), storage  
 298 correction (Lorrai et al. 2010, Rheuban et al. 2014a. Long and Nicholson 2018), non-steady state  
 299 condition bias (Holtappels et al. 2013), slow sensor response time correction (McGinnis et al.  
 300 2008), stirring sensitivity correction (Holtappels et al. 2015), and platform motion corrections  
 301 (Long and Nicholson 2018) have been described and applied, and are discussed elsewhere, as  
 302 noted.

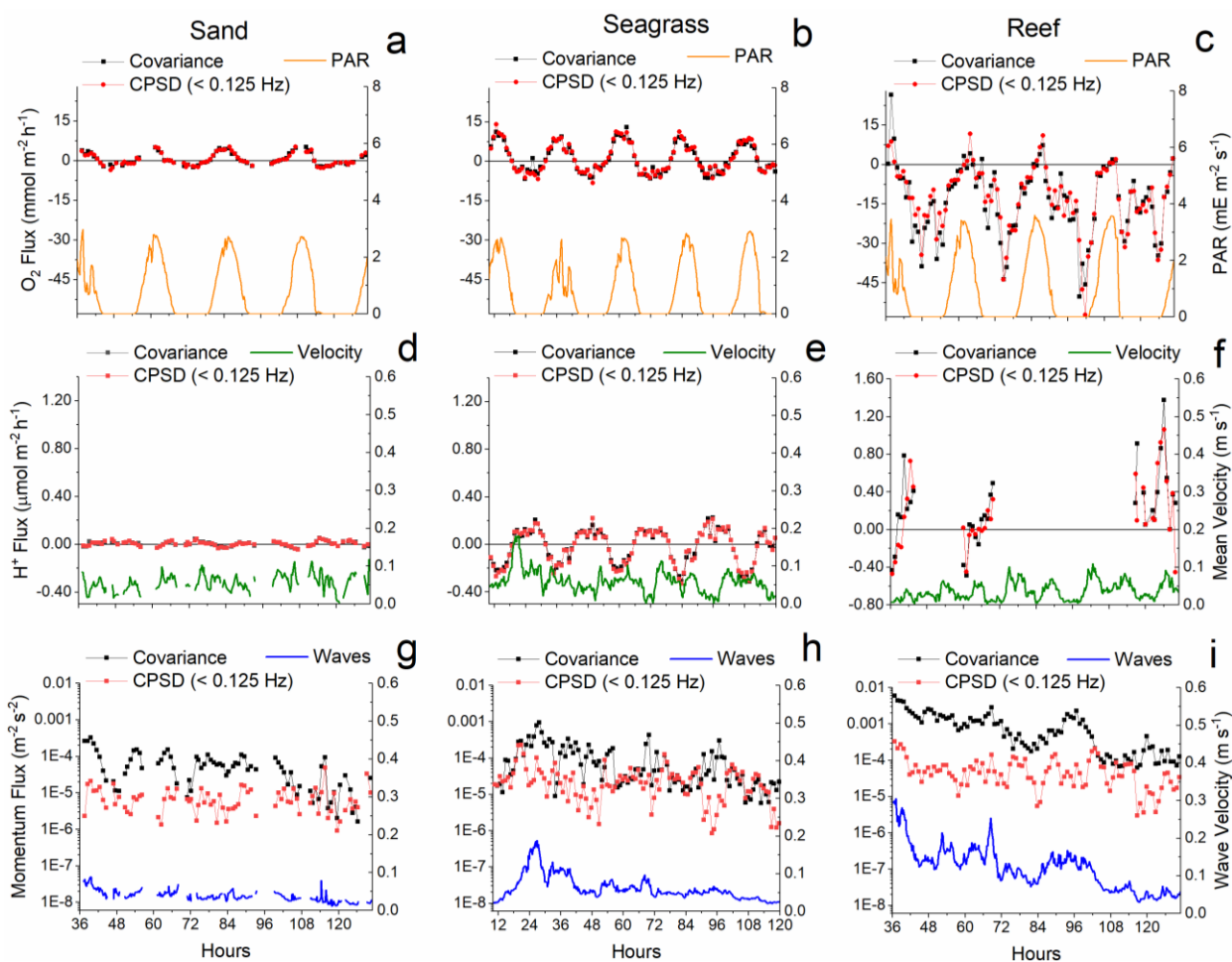
303 *3.2 Field Data* – The three ECHOES and associated instruments were deployed for 4 - 4.5 days at  
 304 each site (sand 96 h, seagrass 108 h, and reef 96 h; Figure 3) with a total of 84h of overlap where  
 305 all 3 ECHOES were collecting data at the same time. In these relatively clear sub-tropical waters  
 306 the ADV velocity beam correlation was used to remove time periods where the correlation was  $<$   
 307 50 % which resulted in the removal of 35.4% (34 h), 0.1% (0.75 h), and 2.3% (4.25 h) of the data  
 308 from the sand, seagrass, and reef sites, respectively (Table 2). At the reef site a substantial amount  
 309 of pH data was lost due to sporadic electrical issues that contaminated 72.4% (69.5 h) of the data.  
 310 Fluxes showed expected diel trends with  $\text{O}_2$  production and  $\text{H}^+$  consumption during the day and  
 311  $\text{O}_2$  consumption and  $\text{H}^+$  production during the night (Figure 3a-f). Biogeochemical fluxes were  
 312 about an order of magnitude larger on the reef site compared to the sand site. Current velocities  
 313 were dominated by diurnal tides and wave velocities generally decreased over the deployment  
 314 period (Figure 3d-i). Diel ranges of  $\text{O}_2$  (171 to 237  $\mu\text{mol L}^{-1}$ ) and pH (8.06 to 8.17) were very  
 315 similar between the adjacent sites.

Table 2. Comparison of direct covariance, CPSD(All Hz), and CPSD (<0.125 Hz) fluxes

Flux	Site	n	Covariance vs. CPSD (All Hz)			Covariance vs. CPSD (<0.125 Hz)		
			Slope ( $\pm$ SE)	R <sup>2</sup>	NRSME	Slope ( $\pm$ SE)	R <sup>2</sup>	NRSME
Oxygen	Sand	248	1.02 $\pm$ 0.01	0.996	1.0 $\pm$ 0.9 %	0.91 $\pm$ 0.01	0.946	2.7 $\pm$ 5.5 %
	Seagrass	429	1.03 $\pm$ 0.00	0.997	0.8 $\pm$ 0.6 %	0.89 $\pm$ 0.02	0.883	2.9 $\pm$ 8.0 %
	Reef	375	1.02 $\pm$ 0.01	0.993	0.7 $\pm$ 0.7 %	0.57 $\pm$ 0.03	0.543	4.1 $\pm$ 10.2 %
	Total	1052	1.02 $\pm$ 0.00	0.994	0.3 $\pm$ 0.9 %	0.66 $\pm$ 0.02	0.644	1.7 $\pm$ 10.8 %
H <sup>+</sup>	Sand	248	1.03 $\pm$ 0.01	0.957	2.5 $\pm$ 1.8 %	0.62 $\pm$ 0.03	0.590	7.2 $\pm$ 5.8 %
	Seagrass	429	1.03 $\pm$ 0.00	0.998	0.5 $\pm$ 0.5 %	0.93 $\pm$ 0.01	0.970	1.3 $\pm$ 2.1 %
	Reef	106	1.03 $\pm$ 0.03	0.920	1.4 $\pm$ 7.1 %	0.87 $\pm$ 0.05	0.738	3.1 $\pm$ 9.1 %
	Total	783	1.03 $\pm$ 0.01	0.945	0.2 $\pm$ 5.6 %	0.88 $\pm$ 0.02	0.788	0.5 $\pm$ 8.2 %
Momentum	Sand	248	1.00 $\pm$ 0.00	0.999	0.2 $\pm$ 0.6 %	0.03 $\pm$ 0.00	0.479	5.0 $\pm$ 21.5 %
	Seagrass	429	1.00 $\pm$ 0.00	0.999	0.2 $\pm$ 0.6 %	0.00 $\pm$ 0.01	0.001	5.7 $\pm$ 24.0 %
	Reef	375	1.01 $\pm$ 0.00	0.999	0.2 $\pm$ 0.6 %	0.03 $\pm$ 0.00	0.542	10.4 $\pm$ 20.5 %
	Total	1052	1.01 $\pm$ 0.00	0.999	0.1 $\pm$ 0.6 %	0.04 $\pm$ 0.00	0.523	4.3 $\pm$ 22.9 %

316

317



318

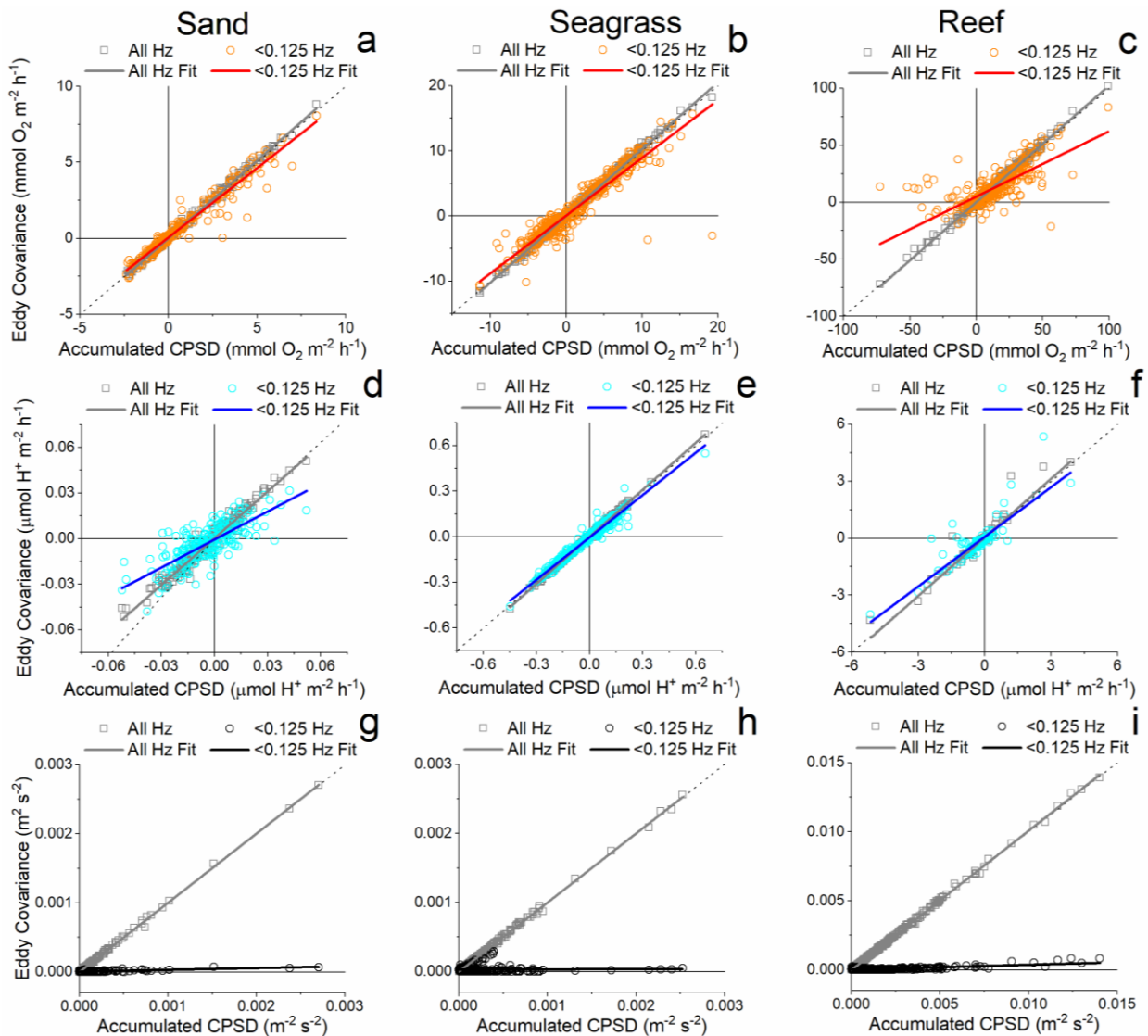
319

320

Figure 3. Time series data and fluxes at sand, grass, and reef sites beginning at noon (hour 12) on June 24, 2018. Oxygen (left a, b, c), H<sup>+</sup> (left d, e, f) and momentum (left g, h, i) fluxes determined

321 by eddy covariance (black) and cross-power spectral densities accumulated below wave  
 322 frequencies ( $< 0.125$  Hz, red). Time series of photosynthetically active radiation (PAR, orange; a,  
 323 b, c), mean velocities (green; d, e, f) and wave velocities (blue; g, h, i) are shown on the right axes.

324 Applying Eq. 3 to the study conditions suggests that there was a spectral gap between wave  
 325 and turbulent frequencies (i.e. Eq. 3  $> 3.1$ , Table 1). Before applying this theory, the agreement  
 326 between fluxes calculated using traditional direct covariance analysis (e.g. Eq. 1) was compared  
 327 to that of the Matlab CPSD function, accumulated across all frequencies. Across the sites (sand,  
 328 grass, and reef) and scalars ( $O_2$ ,  $H^+$ , momentum) the minimum  $R^2$  was 0.92 with a maximum of  
 329 2.5 % normalized root square mean error (NRSME, Table 2, Figure 4). These lowest values were  
 330 found for the scalar with the least data ( $n = 108$  bursts, Reef  $H^+$ , Table 2) and the site with the least  
 331 data and smallest fluxes ( $n = 248$  bursts, Sand  $H^+$ , Table 2, Figure 3d), respectively. The remaining  
 332 majority of results had coefficients of determination of  $\geq 0.99$  and  $\leq 1.0$  % error (Table 2)  
 333 indicating good agreement between direct covariance and CPSD methods (Figure 4).



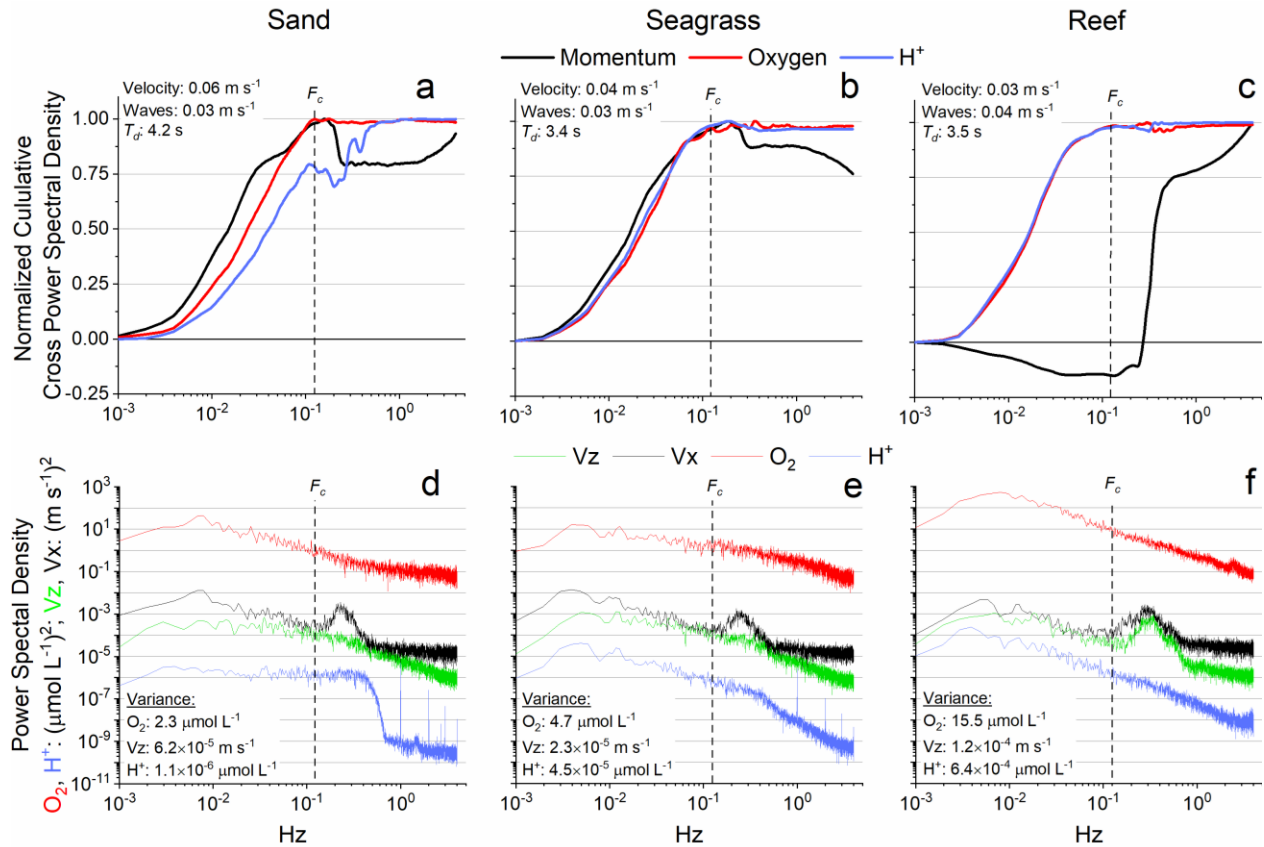
334  
 335 Figure 4. Comparison of fluxes determined from the cross-power spectral densities, accumulated  
 336 across all frequencies, and fluxes determined from eddy covariance (grey boxes, grey lines, a-i)

337 for the sand, grass, and reef sites. The comparison of fluxes determined from cross-power spectral  
338 densities, accumulated up to the wave frequency ( $< 0.125$  Hz), and fluxes determined from eddy  
339 covariance are shown for  $O_2$  (orange circles and red lines, a-c),  $H^+$  (cyan circles and blue lines, d-  
340 f), and momentum (black circles and black lines, g-i) fluxes. Each symbol represents an individual  
341 15 min burst and all lines are linear regressions with statistics reported in Table 2.

342 The wave period ( $T_d$ ) at the sand, grass, and reef sites were  $4.0 \pm 0.5$  (3.1 to 5.7 range),  $3.9$   
343  $\pm 0.5$  (2.6-5.2 range) and  $3.7 \pm 0.6$  (2.0-5.3 range) s, respectively. By examining the power spectral  
344 density of the horizontal velocity (e.g. Figure 5d-f, Figure 6 d-f), especially during periods of high  
345 wave velocity and long wave periods, a cutoff frequency ( $F_c$ ) of 0.125 Hz (8 seconds) was chosen  
346 as the frequency up to which the CPSD should be accumulated to remove wave bias (Figure 5, 6).  
347 In all cases (scalars and sites) the coefficients of determination and slopes were reduced and the  
348 error increased indicating that the frequencies associated with the waves were contributing to the  
349 flux (Table 2). The maximum decrease in the slopes (44%) and error ( $7.2 \pm 5.8$  %) was modest for  
350 the  $O_2$  and  $H^+$  fluxes compared to the substantial decrease in the slope (99%) and increase in error  
351 and variance ( $10.4 \pm 20.5$ ) for the momentum fluxes (Table 2, Figure 4). During periods of low  
352 wave activity, the accumulated CPSD commonly reached a distinct peak or plateau before the  $F_c$   
353 under low wave conditions and had little impact on biogeochemical fluxes (Figure 5a-c). In the  
354 majority of cases, the momentum flux exhibited significant bias at wave frequencies (Figure 4h-j,  
355 Figure 5a-c, Figure 6 a-c). During conditions when the wave velocities were at least twice as high  
356 as the mean flow (occurring 7.3 %, 12.3 % and 66.5 % of the time at the sand, grass and reef sites,  
357 respectively) there was substantial contributions to all of the fluxes at wave frequencies (i.e. Figure  
358 6 a-c). This was most evident during extreme conditions at the reef site, where the wave velocities  
359 were an order of magnitude greater than the current velocity (Figure 6c). The wave velocities were  
360 10-fold greater than the mean velocity 18.1 % of the time at the reef site but were never 10-fold  
361 greater than the mean velocity at the sand and grass sites. Oxygen and  $H^+$  power spectra (Figure  
362 5, 6) showed no variability at wave frequencies while horizontal and vertical velocity spectra  
363 indicated a significant power at wave frequencies (Figure 5, 6). Further, differences between sites  
364 and sampling heights (i.e. sand, 0.35 m sampling height, Figure 5d, 6d) indicated substantial power  
365 at wave frequencies predominantly in the horizontal spectra, where wave orbitals become  
366 compressed vertically when sampling closer to the bottom, while the reef (0.97 m sampling height)  
367 indicate a balance between power at wave frequencies in both the horizontal and vertical (Figure  
368 5f, 6f). Across the sites, the absolute differences between the hourly eddy covariance and CPSD  
369 fluxes (i.e. Figure 3a-c) were positively correlated to the wave velocity with slopes significantly  
370 different from zero and the strongest coefficient of determination for the momentum flux ( $R^2 =$   
371  $0.71$ ) followed by the  $O_2$  flux ( $R^2 = 0.32$ ), and  $H^+$  flux ( $R^2 = 0.06$ ) (Figure S3).

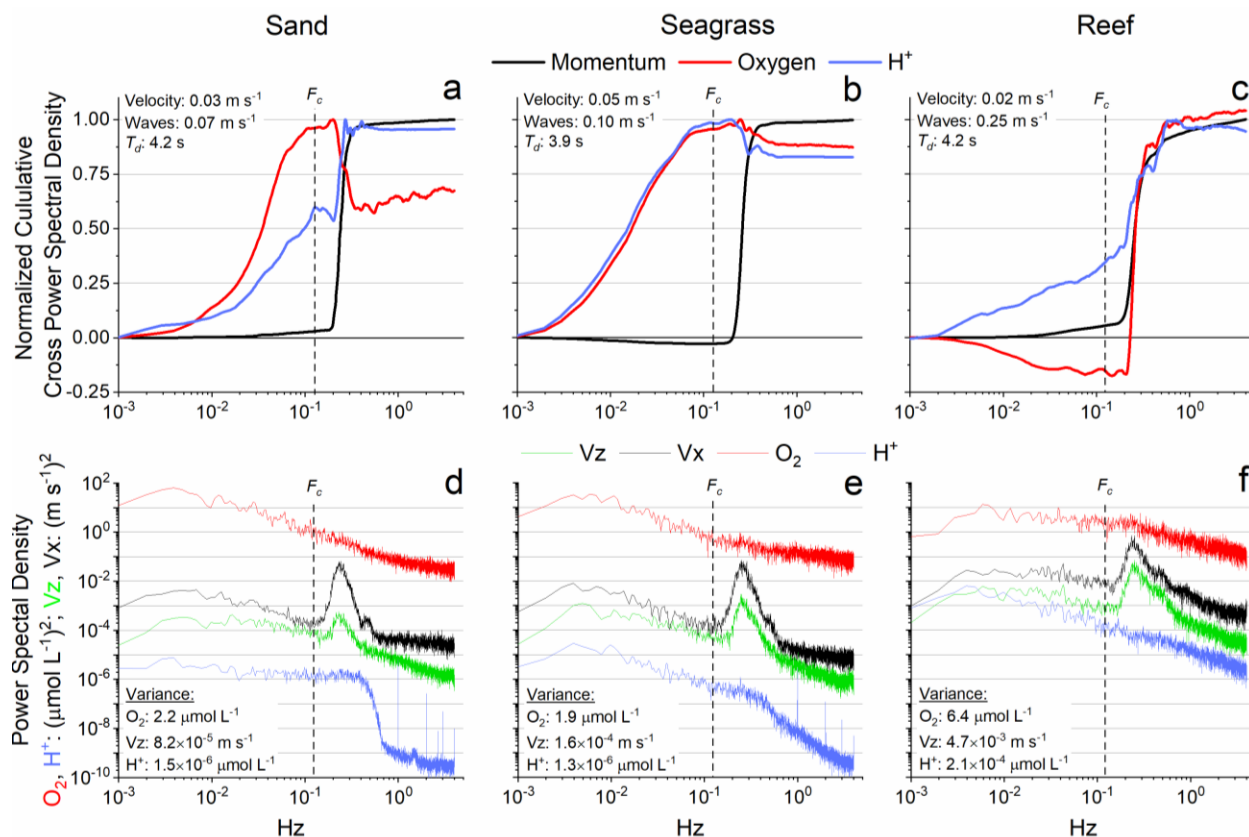
372

373



374

375 **Figure 5:** Spectral data from a low wave-energy period (hour 116, Figure 3). Normalized  
 376 cumulative cross-power spectral densities show distinct differences between momentum fluxes  
 377 and biogeochemical fluxes at wave frequencies. Oxygen and H<sup>+</sup> spectra (lower panels, red and  
 378 blue, respectively) show no variability at wave frequencies while horizontal (V<sub>x</sub>, black) and  
 379 vertical velocity (V<sub>z</sub>, green) spectra indicate a significant power at wave frequencies. Further,  
 380 differences between sites and sampling heights (i.e. sand, 35cm sampling height) indicate  
 381 substantial power at wave frequencies in the horizontal spectra, where wave orbitals become  
 382 compressed vertically when sampling closer to the bottom, while the reef (lower right, 97cm  
 383 sampling height) indicate a balance between power at wave frequencies in both the horizontal and  
 384 vertical. Mean current velocities, wave velocities, and wave period are shown in text where wave  
 385 and current velocities were of the same order of magnitude (a-c). The variance of oxygen, vertical  
 386 velocity, and H<sup>+</sup> (text, d-f) over each period indicate an increase in both biogeochemical tracer and  
 387 vertical turbulence variances from the sand to reef sites.



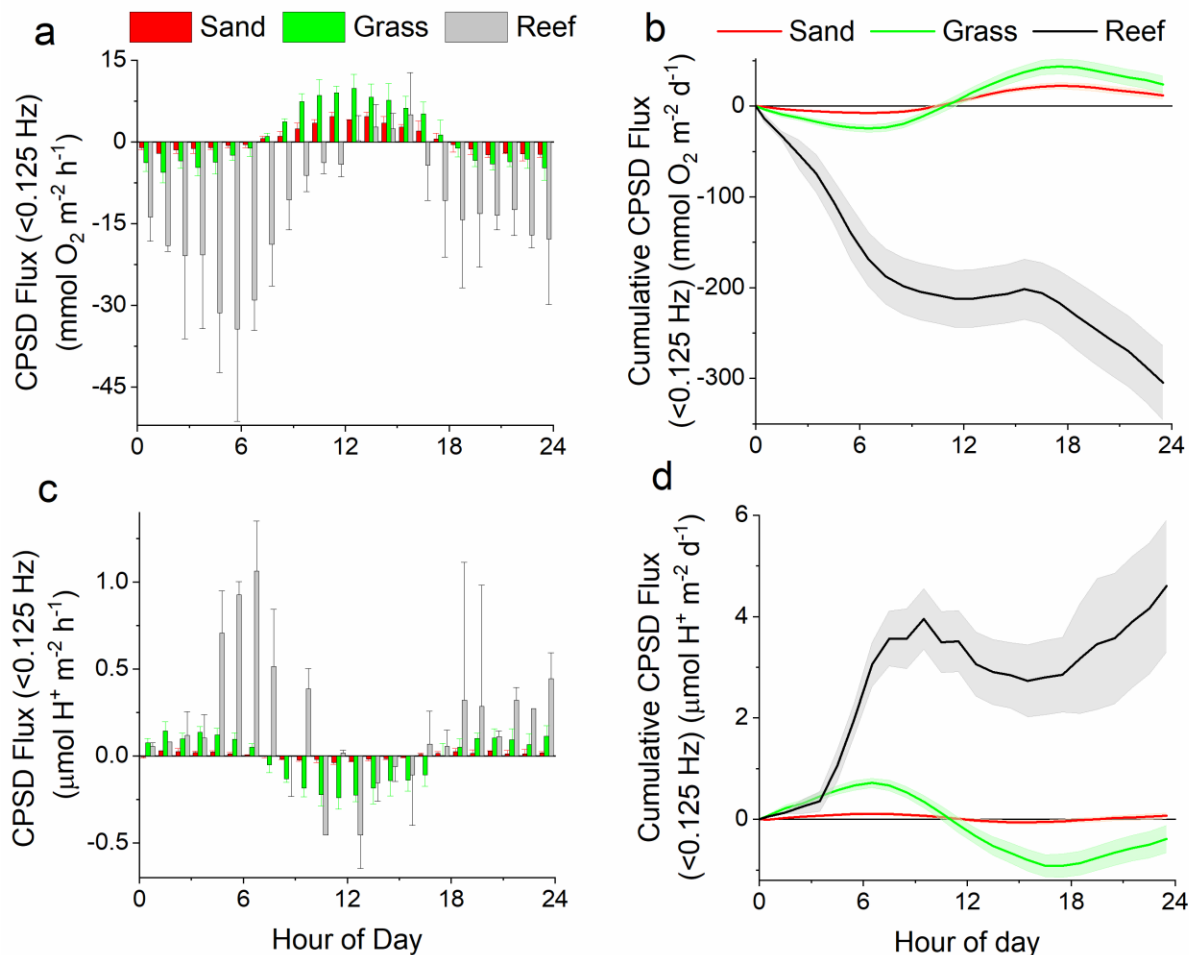
388

389 **Figure 6:** Spectral data from a high wave-energy period (hour 38, Figure 3). Cumulative cospectral  
 390 densities show distinct differences between momentum fluxes and biogeochemical fluxes. Oxygen  
 391 and  $H^+$  spectra (lower panels, red and blue, respectively) show no variability at wave frequencies  
 392 while horizontal ( $V_x$ , black) and vertical velocity ( $V_z$ , green) spectra indicate a significant bias by  
 393 waves. Further, differences between sites and sampling heights (i.e. sand, 35cm sampling height)  
 394 indicate substantial power at wave frequencies in the horizontal spectra, where wave orbitals  
 395 become compressed vertically when sampling closer to the bottom, while the reef (lower right,  
 396 97cm sampling height) indicate a balance between power at wave frequencies in both the  
 397 horizontal and vertical and potential bias in the cospectra of the biogeochemical fluxes (a-c). Mean  
 398 current velocities, wave velocities, and wave period are shown in text where wave velocities were  
 399 twice as large as the current velocities at the sand and grass sites (a-b) and an order of magnitude  
 400 larger at the reef site (c). The variance of oxygen, vertical velocity, and  $H^+$  (text, d-f) over each  
 401 period indicate an increase in both biogeochemical tracer and vertical turbulence variances from  
 402 the sand to reef sites.

403 **3.3 Ecosystem Fluxes** - The hourly  $O_2$  and  $H^+$  CPSD ( $<0.125$  Hz) fluxes across each deployment  
 404 (Figure 3a-f) were averaged by hour of day (Figure 7a, c) to enable the calculation of net daily  
 405 fluxes averaged over the  $\sim 4$  day deployments (Figure 7b, d). The method of calculation of net  
 406 ecosystem metabolic (NEM) rates (e.g. Rheuban et al. 2014a) was chosen due to the significant  
 407 data gaps in the sand  $O_2$  and  $H^+$  and reef  $H^+$  fluxes (Figure 3). Both sand and seagrass sites  
 408 exhibited net positive  $O_2$  fluxes and autotrophy ( $11.8 \pm 4.1$  and  $23.8 \pm 9.2$  mmol  $O_2$   $m^{-2}$   $d^{-1}$ ,  
 409 respectively) while the reef site had net negative  $O_2$  fluxes and strong heterotrophy ( $-304.8 \pm 40.9$   
 410 mmol  $O_2$   $m^{-2}$   $d^{-1}$ ) (Figure 7b). The seagrass site had net negative  $H^+$  fluxes indicating a  
 411 consumption of acidity ( $-0.39 \pm 0.26$   $\mu\text{mol } H^+$   $m^{-2}$   $d^{-1}$ ), the sand site had near-balanced  $H^+$  fluxes

412 indicating no significant net production or consumption of acidity ( $0.07 \pm 0.06 \mu\text{mol H}^+ \text{m}^{-2} \text{d}^{-1}$ ),  
 413 and the reef site had net positive  $\text{H}^+$  fluxes indicating significant net acidity production ( $4.61 \pm$   
 414  $1.30 \mu\text{mol H}^+ \text{m}^{-2} \text{d}^{-1}$ ) (Figure 7d).

415



416

417 Figure 7. Accumulated cross power spectral density (<0.125 Hz) O<sub>2</sub> (a) and H<sup>+</sup> (c) fluxes averaged  
 418 by hour of day from all data in Figure 3a-f for sand (red), seagrass (green) and reef (grey) sites.  
 419 The fluxes were accumulated across the hour of day, where shading indicates propagated error, to  
 420 produce a net daily O<sub>2</sub> (b) and H<sup>+</sup> (d) fluxes for each site.

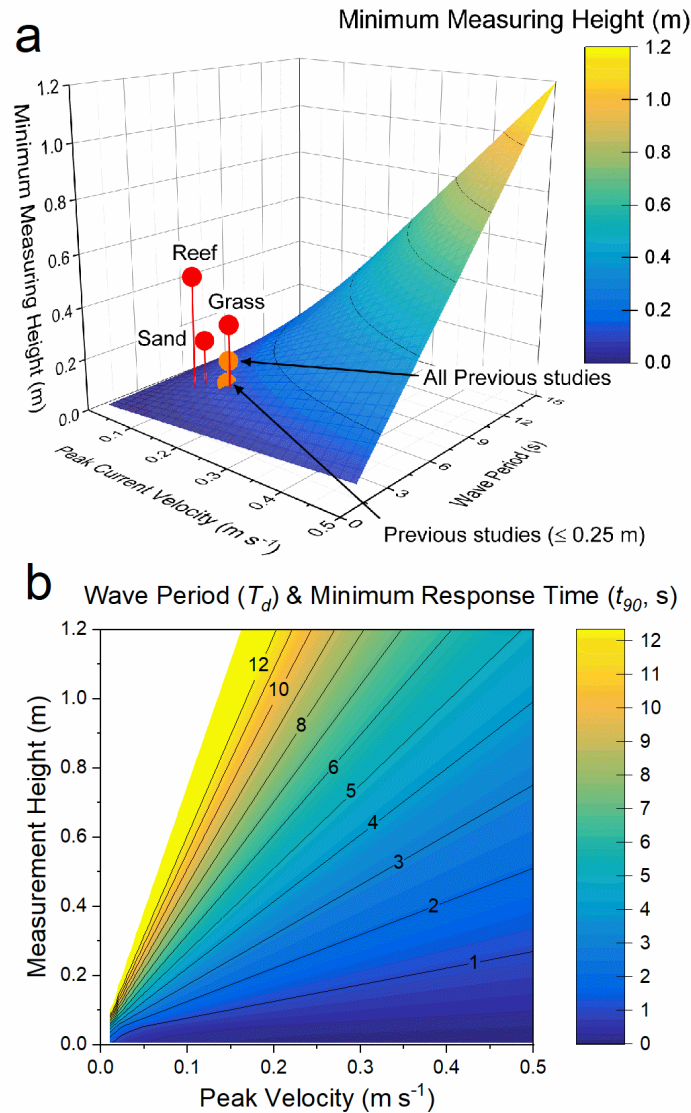
421

#### 422 **4 Discussion**

423 This research presents a new analysis framework and measurement requirements to enable  
 424 biogeochemical EC measurements in the presence of waves. Since most studies using the EC  
 425 technique have been conducted in shallow waters where waves are common, this has represented  
 426 a significant setback for the small, but rapidly expanding biogeochemical EC community.  
 427 Essentially, by measuring higher above the boundary than has been done traditionally (mostly <  
 428 0.25 m), the turbulent frequencies shift to longer scales, above the wave frequencies. The presented  
 429 spectral analyses framework has been used to calculate turbulent fluxes by filtering out wave

430 frequencies and has demonstrated that there is a clear spectral gap between the frequency of the  
431 dominant surface waves and the dominant frequencies of the turbulent flux when measurements  
432 are conducted at sufficient distance away from the interface (Scully et al. 2016). Here, spectral  
433 analysis reveals conditions and measurement heights that produce gaps between turbulence and  
434 wave frequencies in both scalar (e.g. O<sub>2</sub> and H<sup>+</sup>) and turbulence measurements. Therefore, waves  
435 can be spectrally filtered and effectively remove bias in both chemical sensor and turbulence  
436 measurements, which also allows for new EC chemical sensors that have slower response times to  
437 be applied to the EC technique.

438 *4.1 Literature review* – The review of field-based biogeochemical EC studies revealed that the  
439 majority of studies have been conducted in shallow environments where waves are likely to occur.  
440 This potential for wave bias is compounded by the fact that the majority of studies (78%) used  
441 Clark-type microsensors, that have known biases created by wave-associated velocities and  
442 frequencies (Donis et al. 2015, Holtappels et al. 2015, Berg et al. 2015, Reimers et al. 2016a). The  
443 majority of studies sampled < 0.25 m from the bottom boundary (69%, 0.12 m mean when  
444 corrected for roughness elements) and it is likely that many of these studies would not exhibit a  
445 clear separation between wave and turbulence frequencies, as described in Eq. 3, which is  
446 illustrated by the color-mapped surface in Figure 8a. However, it is apparent that some previous  
447 studies could benefit from the presented spectral analysis framework, and that using higher  
448 measurement heights will benefit future studies (e.g. Figure 8b).



449

450 **Figure 8:** Minimum sampling heights that allow for a distinct gap between turbulence and waves  
 451 frequencies based on  $(2\pi z)/(UT_d) = 1$  (Eq. 3, Scully et al. 2016) (a). Individual points show  
 452 sampling heights over sand, grass, and reef sites in this study minus the characteristic roughness  
 453 heights of 0.1 (bedforms), 0.2 (seagrass canopy), and 0.5 m (reef canopy), respectively (red dots,  
 454 Table 1). The Mean of Previous Studies represents the average measurement heights and peak  
 455 current velocities (and an assumed  $T_d$  of 4 s) from the all previous studies and those conducted  
 456 with a measurement height of  $< 0.25$  m in Figure 1 (orange dots, Table 1). Rearranging the equation  
 457  $(2\pi z)/(UT_d) = 3.1$  (the minimum value demonstrated in this study to allow for separation of  
 458 turbulence and wave frequencies) to solve for  $T_d$  and color shading by the assumption that the  
 459 minimum response time is approximately the  $T_d$  (or the Nyquist frequency ( $2x$ ) of the cutoff  
 460 frequency [ $F_c \approx 1/(2T_d)$ ]), produces a recommended minimum response time ( $t_{90}$ , b) based on site  
 461 conditions.

462 **4.2 CPSD analyses framework** – The presented CPSD analysis framework begins with a careful  
 463 consideration of the site conditions, which inform appropriate measurement heights to allow for  
 464 the spectral separation of turbulence and waves. When data is collected at appropriate

465 measurement heights, the data can then be analyzed in the frequency domain, where the CPSD can  
466 be used to determine fluxes and wave periods can be evaluated. This spectral analyses can then be  
467 used to remove wave frequencies, by accumulating the CPSD up to the wave frequencies,  
468 effectively removing sensor and turbulence wave biases. Accumulating the CPSD across all  
469 frequencies can be used to compare with standard eddy covariance analyses, as well as determining  
470 the contribution to fluxes at wave frequencies. While this method is mostly applicable to sites with  
471 high frequency surface waves and moderate current velocities, it is noted that these are the  
472 predominate conditions for most biogeochemical eddy covariance studies to date.

473 The presented CPSD method, when accumulated across all frequencies, showed a very  
474 good agreement with traditional eddy covariance analysis with slopes of 1.0,  $R^2 \geq 0.92$ , and error  
475  $\leq 2.5\%$ , where the lowest  $R^2$  and highest error were found for  $H^+$  fluxes with the least data and  
476 smallest fluxes, respectively. When the CPSD was accumulated only up to the wave frequencies  
477 (i.e. the cutoff frequency,  $F_c$ ) there was a decrease in the flux in all cases, with a substantial  
478 decrease in the momentum flux, followed by less pronounced decreases for the biogeochemical  
479 tracers of  $O_2$  and  $H^+$ . The large decrease in the momentum flux is expected as waves bias both  
480 horizontal and vertical velocities that are used to calculate the momentum flux, while  $O_2$  and  $H^+$   
481 sensors are not affected at wave frequencies as they are located in a microfluidic housing that  
482 removes wave velocities by placing the sensors in a constant-flow environment. However, wave  
483 bias is still present during high-wave periods due to the vertical velocities used to calculate the  
484 biogeochemical fluxes, albeit much lower than the momentum fluxes that includes both horizontal  
485 and vertical wave components.

486 The fluxes generally reached a maxima or plateau before reaching the  $F_c$ , demonstrating  
487 the relationship in Eq. 3, where there is a distinct spectral gap between the turbulence and wave  
488 frequencies. During extreme wave conditions at the reef site, where current velocity was 10-fold  
489 lower than wave velocities, this was not always apparent (e.g. Figure 6c), but this is likely due to  
490 the limited cross-power spectral density at these low current velocities (i.e. the relatively flat  
491 velocity spectra at turbulence frequencies,  $<0.125$  Hz), as opposed to wave bias, as the spectra  
492 clearly show the wave frequencies well above the  $F_c$ . Further, if wave and turbulent frequencies  
493 overlap during some study periods, for example during periods of low wave frequency (or high  
494  $T_d$ ) and high current velocity, it is straightforward to exclude these data from analysis based on Eq.  
495 3.

496 In a previous study by this author, Long et al. (2015c), the presented cumulative  
497 cospectrum (Figure 8f in Long et al 2015c) illustrate an ideal application of the presented CPSD  
498 methodology, as there is a distinct separation between the turbulence and wave frequencies. In this  
499 example the measurement height was 0.175 m (0.35 m measurement height - 0.175 m seagrass  
500 canopy height), flow velocities were very low ( $0.011 \text{ m s}^{-1}$ ) and wave periods were very fast ( $\sim 1.4$   
501 s) (Long et al. 2015c). Applying these parameters to Eq. 3 results in a value of 71.4, suggesting a  
502 substantial gap between turbulence and wave frequencies, which is apparent in the cumulative  
503 cospectrum that indicate a flux plateau and stable maximum from 0.1 Hz up to the wave  
504 frequencies ( $\sim 0.5$  to 1 Hz). In another EC study, by Kuwae et al. (2006), where current velocities  
505 from  $\sim 0.1$  to  $0.2 \text{ m s}^{-1}$ , wave periods of 1-4 seconds, and measurement heights of 0.07 to 0.17 m  
506 produced values of Eq 3. of 0.6 to 10.7, suggesting that the CPSD method could also be applied to  
507 their study site. Kuwae et al. (2006) shows cumulative spectra and cospectra that 1.) illustrate  
508 wave-biased vertical velocity spectrum with no effect in  $O_2$  spectrum, 2.) a typical turbulence-  
509 dominated cumulative cospectrum with frequencies from 0.01 to a stable maxima at 0.2 Hz and a

510 negative contribution at 1-2 Hz, and 3.) cumulative cospectra that indicate significant contributions  
511 at wave frequencies from 0.2 to 1 Hz. These examples from Kuwae et al. (2006) are similar to the  
512 full-frequency spectra and cospectra presented in this study, notably for 1.) Figure 5, 6 e-f, 2.)  
513 Figure 6a-c, and 3.) Figure 6c. These previous studies were conducted with Clark-type  
514 microsensors which have been shown to be biased by wave orbital velocities (Berg et al. 2015,  
515 Donis et al. 2015, Holtappels et al. 2015, Reimers et al. 2016a) but these previous studies also  
516 suggest that wave velocities may cause scalar transport through the advection of porewater (Kuwae  
517 et al. 2006) or advection of turbulent motions or scalar variances through a fixed measurement point  
518 (Lumley and Terray 1983, Gerbi et al. 2008, Long et al. 2015c, Long and Nicholson 2018).  
519 Whether these wave-frequency variations are due to sensor biases (e.g. Holtappels et al. 2015,  
520 Reimers et al. 2016a), instrument orientation or tilt biases (e.g. Trowbridge 1998, Scully et al.  
521 2016), or are actual transport at wave frequencies (Lumley and Terray 1983, Kuwae et al. 2006,  
522 Gerbi et al. 2008), the presented CPSD method, in combination with appropriate measurement  
523 heights, provides a specific framework to separate turbulent and wave-associated fluxes to  
524 overcome these biases, or to quantify fluxes associated with wave frequencies.

525 *4.3 Sensors and Waves* – The spectra for O<sub>2</sub> and H<sup>+</sup> do not show variability associated with the  
526 wave peaks present in the vertical and horizontal spectra, even during extreme wave conditions at  
527 the reef site. This suggests that the microfluidic sensor housing effectively removed wave bias  
528 from the sensors (Long and Nicholson 2018). The active pumping past the sensors created a  
529 constant-flow environment negating zero-crossing velocities and removed any concerns related to  
530 boundary layer, wave and pressure fluctuations and associated sensor response times (see Reimers  
531 et al. 2016a). These optical O<sub>2</sub> and H<sup>+</sup> ion selective field effect transistors (ISFET) sensors are  
532 sensitive to light interference (Long et al. 2015a) and therefore benefited from the darkened  
533 housing, although light interference for the O<sub>2</sub> optode only occurs in very shallow water due to its  
534 use of red light that is quickly attenuated with water depth. The rotating base allowed the precise  
535 correction for the separation between the sensors (Donis et al. 2015, Holtappels et al. 2015,  
536 Reimers et al. 2016a) using the known sensor separation, flow rate and the fact that that sensors  
537 were always oriented in line with the flow (Long et al. 2019). The Inertial Measurement Unit  
538 (IMU, housing a triaxial accelerometer, gyroscope, and magnetometer) measured the exact  
539 instrument orientation, movement and acceleration to allow for coordinate matrix transformation  
540 to account for platform rotation and movement (Long and Nicholson 2018). This new instrument  
541 design and motion correction is based on similar advancements used in atmospheric ship-based  
542 eddy covariance measurements to correct for ship motion (e.g., Edson et al. 1998, McGillis et al.  
543 2001, Flügge et al. 2016).

544 This ECHOES measurement system including microfluidics (Long et al. 2015a) and IMU  
545 integration (Long and Nicholson 2018) represents a significant advancement of the EC technique  
546 that allow it to overcome previous challenges related to sensor wave bias and sensor separation  
547 corrections (Donis et al. 2015, Holtappels et al. 2015, Berg et al. 2015, Reimers et al. 2016b).  
548 However, while this ECHOES instrument design removed concerns related to sensor wave bias, it  
549 also complicated instrument engineering, had additional power requirements due to the use of a  
550 pump, and may not effectively rotate at very low current velocities. Importantly, this instrument  
551 configuration cannot remove bias in the vertical velocities used to calculate the flux. Thus, the  
552 presented combination of methodological improvements and the CPSD analysis framework is  
553 preferable to effectively remove wave bias from EC flux measurements. However, future studies  
554 applying O<sub>2</sub> optodes, O<sub>2</sub> Clark-type microsensors, or other sensors in a traditional, fixed, open-  
555 sensor EC instrument (e.g. Berg et al. 2003) will still benefit substantially from the CPSD analysis

556 framework by removing wave bias caused by sensor sensitivity to wave velocities as well as  
557 removing wave frequencies that can cause bias in sensor separations corrections.

558 This manuscript presents the first use of a Honeywell Durafet® III pH sensor in an EC  
559 instrument. The reduction of noise in the signal was a major initial challenge with good results  
560 produced by using an optically coupled power supply and amplifier. However, it was still apparent  
561 that there was low density in the power spectra across frequencies, especially at the sand site. This  
562 is exhibited in the fairly flat power spectral density and low variance for the sand site (Figure 5d,  
563 6d) and may indicate a lower threshold for resolving the  $H^+$  flux (sand site,  $\pm 0.03 \mu\text{mol m}^{-2} \text{h}^{-1}$ )  
564 whereas fluxes were about an order of magnitude larger at the seagrass and reef sites. This lower  
565 resolution for the  $H^+$  data was also apparent in the highest error and lowest coefficients of  
566 determination when comparing the full-spectrum CPSD and EC flux calculation methods.  
567 However, the use of  $H^+$  ISFET sensors (along with  $O_2$  sensors) is promising as a biogeochemical  
568 tracer due to its ability to be used in carbonate chemistry models to determine rates of calcification  
569 and dissolution (Long et al. 2015a, Takeshita et al. 2016).

570 *4.4 Ecosystem Fluxes* - The determined fluxes across the sites showed expected diel trends with  
571 generally positive  $O_2$  fluxes during the daytime and negative  $O_2$  fluxes at night. The  $H^+$  fluxes  
572 showed the opposite diel trend, consistent with  $CO_2$  consumption by photosynthesis during the  
573 day and  $CO_2$  production by respiration at night. Both seagrass and sand  $O_2$  fluxes exhibited net  
574 autotrophy, but the reef site showed strong heterotrophy likely due to the predominance of  
575 octocorals, algae, and rubble at this heavily degraded reef site (Hopkinson et al. 2020, Owens et  
576 al. 2020). Both the seagrass and sand  $O_2$  fluxes are consistent with previous measurements nearby  
577 in a similar depth seagrass meadow by Long et al. (2015b) ( $NEM = 37 \pm 31 \text{ mmol } O_2 \text{ m}^{-2} \text{ d}^{-1}$ ) and  
578 in a slightly deeper sandy site by Berg et al. (2016) (flux range = -2 to 4  $\text{mmol } O_2 \text{ m}^{-2} \text{ h}^{-1}$ ). The  
579 study sites were visited frequently during the afternoon and the production of bubbles was not  
580 observed at these sites, but we cannot conclusively determine that bubble ebullition of  $O_2$  did not  
581 bias the presented  $O_2$  fluxes (see Long et al. 2020). Notably, the reef net heterotrophy found here  
582 is a shift from the net autotrophy or balanced metabolism found nearby at Grecian Rocks Reef in  
583 2009-2010 (Long et al. 2013) and may reflect differences between sites, the continuing degradation  
584 of the northern Florida Keys Reef tract (Muehllehner et al. 2016), and particularly to the  
585 proliferation of a bloom of red algae (*Galaxaura* spp.) following Hurricane Irma in 2017 that  
586 persisted through the time of our measurements in 2018 (Hopkinson et al. 2020, Owens et al.  
587 2020). The  $H^+$  fluxes observed at our sand site ( $\pm 0.03 \mu\text{mol m}^{-2} \text{h}^{-1}$ ) are about an order of  
588 magnitude lower than those found at other biogenic calcium carbonate sandy sites ( $\pm 0.4 \mu\text{mol m}^{-2}$   
589  $\text{h}^{-1}$ , Cyronak et al. 2013) but these previous data were obtained in an isolated lagoon with large  
590 diel pH changes from about 7.8-8.4 that drove changes in dissolution and calcification (Santos et  
591 al. 2011, Cyronak et al. 2013) compared to the much lower diel pH (8.06 to 8.17) at our sand site.  
592 The large  $H^+$  fluxes found at this isolated lagoon ( $\pm 0.4 \mu\text{mol m}^{-2} \text{h}^{-1}$ , Cyronak et al. 2013; -1.1 to  
593  $0.3 \mu\text{mol m}^{-2} \text{h}^{-1}$ , Santos et al. 2011) are more consistent with the magnitude of fluxes that were  
594 observed at our reef site (-0.5 to 1.1  $\mu\text{mol m}^{-2} \text{h}^{-1}$ ). The seagrass site was the only site that acted as  
595 a net acidity sink, consistent with studies that indicate seagrass meadows act as a carbon sink (e.g.  
596 Duarte et al. 2010).

597 *4.5 Guidelines for Measurement Height and Sensor Response Time* – In this study, the ADV and  
598 sensor measurement height above the sediment surface was determined by placing it at a height  
599 that was greater than twice the biological canopy or bedform height (Figure 1, Attard et al. 2014,  
600 Long et al. 2015c) as recommended by terrestrial EC guidelines where twice the canopy height,

601 and up to 5 times the canopy height in patchy environments, is recommended (Burba and Anderson  
602 2010). The resulting values for Eq. 3 ranged from 3.1 to 7.3 based on the site conditions, and it  
603 was evident that being substantially above the relationship suggested by Eq. 3 (e.g. Eq. 3 > 1,  
604 Scully et al. 2016) is beneficial to highlight and resolve the stable maxima produced prior to the  
605 wave frequencies (Figure 5, 6; Long et al. 2015c). Further, it is apparent that some studies sampled  
606 too close to the bottom to allow for spectral turbulence and wave separation as the mean of studies  
607 sampling < 0.25 m from the boundary fall directly on the surface defined by Eq. 3 = 1 (Figure 8a).  
608 Biological canopy heights (e.g. reef structures, macrophyte canopies) and physical roughness  
609 elements (e.g. grain size, bedforms) should also be considered when choosing measurement  
610 heights, as measurement heights are commonly reported from the benthic surface, not the surface  
611 of biological canopies that, in some cases, also vary in height with current velocity when the  
612 canopy is flexible (i.e. seagrasses, Nepf 2012).

613 With the recommended measurement heights, based on current velocities and wave period,  
614 it follows that if the response time of the sensor (typically represented as to the time to reach 90%  
615 of the total signal change) is twice as large as the determined cutoff frequency (i.e. the Nyquist  
616 frequency of  $F_c$ ), the majority of the turbulent flux can be captured. Rearranging the equation  
617  $(2\pi z)/(UT_d) = 3.1$  (or the conservative minimum value demonstrated in this study to allow for  
618 separation of turbulence and wave frequencies) to solve for  $T_d$  and color shading by the assumption  
619 that the minimum response time is approximately the  $T_d$  (or the Nyquist frequency (2x) of the  
620 cutoff frequency [ $F_c \approx 1/2T_d$ ]), produces a recommended minimum response time ( $t_{90}$ ) based on  
621 site conditions (Figure 8b). For example, at a common shallow-water site where current velocity  
622 is  $\leq 0.2 \text{ m s}^{-1}$ ,  $T_d$  is  $\leq 4 \text{ s}$ , and measurements are conducted 0.5 m from the top of the bottom  
623 roughness elements, a sensor with a  $t_{90}$  of  $\sim 5 \text{ s}$  (0.2 Hz) can record all of the contributions to the  
624 CPSD flux accumulated up to the  $F_c$ . However, if the frequencies above the  $F_c$  are of interest due  
625 to potential advection of turbulence or porewater at wave frequencies (e.g. Lumley and Terray  
626 1983, Kuwae et al. 2006, Gerbi et al. 2008), then a sensor that has a response time equivalent to  
627 the 2x the wave frequencies would be required. This role of physical transport at wave frequencies  
628 remains unresolved and requires further study, but is largely outside the main objectives of  
629 biogeochemical EC studies where chemical and turbulence sensor wave-bias is a major  
630 impediment.

631 There are additional factors to consider with sampling higher above the bottom including;  
632 increased bias in the fluxes due to storage within the water column, larger areas of integration,  
633 or footprints, with increased measurement heights (Berg et al., 2003, Attard et al. 2014), increased  
634 time-lag for changes at the benthic surface to reach the measurement point (Rheuban and Berg  
635 2013), and interaction with shear layers or strong concentration gradients during non-steady state  
636 conditions (Holtappels et al. 2013). These factors should be considered when choosing  
637 measurement heights, but can be minimized by sampling over long periods, and are generally small  
638 compared to the potential for wave-bias at shallow sites. For example, changes in storage in the  
639 water column are now commonly included with large measurement heights (Long et al. 2013,  
640 Rheuban et al. 2014a, Berger et al. 2020, Koopmans et al, 2020). Larger footprints are generally  
641 considered beneficial as they integrate benthic heterogeneity (Rheuban and Berg 2013). The time-  
642 lag between when the flux is released at the benthic surface and when it is recorded at the  
643 measurement height can be corrected when correlating fluxes to environmental driving variables  
644 (i.e. irradiance, tides, concentrations) (Rheuban and Berg 2013). Further, the effects of all potential  
645 biases can be reduced by increasing deployment duration, especially over a variety of non-steady  
646 state conditions to better integrate flux estimates through time (Holtappels et al. 2013). Therefore,

647 considering the substantial benefit of sampling higher above the bottom to remove wave bias, and  
 648 the lower risk of other factors above, it is recommended to use adequate measurement heights (e.g.  
 649 Figure 8b) at shallow sites where waves may be present.

650 *4.6 Application to Similar Flux Techniques* - The gradient flux, or profile flux, technique relies on  
 651 the same boundary layer assumptions as the EC technique, but uses measurements of the gradients  
 652 or profile of current velocity and solute concentrations through the boundary layer (McGillis et al.  
 653 2009, McGillis et al. 2011, Turk et al. 2015, Takeshita et al. 2016). Similar to the development of  
 654 aquatic EC, the scalar transport of gas and water fluxes in the marine atmospheric boundary layer  
 655 steered these developments (McGillis et al. 2001, Zappa et al. 2003, Edson et al. 2004). In the  
 656 gradient flux technique, the flux of a solute is calculated as:

$$657 \quad \text{Flux} = -K_z \frac{\partial C}{\partial z} \quad \text{Eq. 4.}$$

658 where  $-K_z$  is the eddy diffusivity, and  $\frac{\partial C}{\partial z}$  is the benthic concentration gradient usually measured  
 659 using a pair of chemical sensors or a dual-height pumping system at known heights ( $z$ ) above the  
 660 bottom (Takeshita et al. 2016). Gradient exchange fluxes are determined by taking the integral of  
 661 Eq.4 across  $\partial z$  and using the relationship  $K_z = u^* \kappa z$  (where  $u^*$  is the friction velocity and  $\kappa$  is  
 662 Von Karman's constant) (McGillis et al. 2009). The resulting relationship [ $\text{Flux} =$   
 663  $u^* \kappa ((C_{z_2} - C_{z_1}) / \log(z_2/z_1))$ ] determines  $u^*$  from logarithmic fits to benthic current profiles,  
 664 which is an assumption that is often problematic in high roughness shallow systems during low  
 665 flow conditions in the presence of waves (Holtappels and Lorke 2011, Nepf 2012, Trowbridge and  
 666 Lentz 2018). The gradient exchange technique has been primarily applied in shallow coastal  
 667 seagrass and reef ecosystems (McGillis et al. 2009, Turk et al. 2015, Takeshita et al. 2016) and  
 668 could benefit from the new analysis framework applied here by the direct calculation of  $K_z$ .  
 669 Assuming a Prandtl number of 1, the eddy diffusivity can be calculated by:

$$670 \quad K_z = (\overline{u'w'}) / \frac{\partial U}{\partial z} \quad \text{Eq. 5.}$$

671 where  $(\overline{u'w'})$  is the momentum flux (e.g. Eq. 1) and  $\frac{\partial U}{\partial z}$  is the shear calculated from a velocity  
 672 profile of mean flow (Holtappels and Lorke 2011). Using the CPSD accumulation for determining  
 673 the momentum fluxes will yield direct measurements of  $K_z$ , which is superior to the assumption  
 674 of a logarithmic boundary layer current profile, especially in high-roughness shallow environments  
 675 (Holtappels and Lorke 2011) such as coral reefs and seagrass beds where flow profiles often do  
 676 not follow a logarithmic relationship (Nepf 2012). For example, the momentum fluxes calculated  
 677 from traditional covariance analysis produced substantially larger values (Table 2, Figure 4) and  
 678 accumulating the CPSD below the wave frequencies will enable a more accurate determination of  
 679  $K_z$  for the gradient exchange technique while removing the need to assume a logarithmic boundary  
 680 layer current profile.

681

## 682 **5 Summary**

683 The review of aquatic biogeochemical EC literature has revealed that biases created by  
 684 waves have complicated the use of aquatic EC in shallow waters at a time when coastal processes  
 685 are gaining recognition as important factors in nearshore water quality, regional biogeochemical  
 686 cycles and global modeling efforts. However, the conditions and instrument configurations used  
 687 during previous studies suggest that a fundamental shift in how EC measurements are conducted

688 and analyzed can overcome these limitations. The new analysis framework presented here,  
689 including using appropriate measurement heights and CPSD accumulation up to wave frequencies,  
690 demonstrates and that full-spectrum CPSD analysis is consistent with traditional EC analysis, and  
691 that wave-bias apparent in traditional EC analysis can be removed through exclusion of waves  
692 frequencies using spectral CPSD accumulation. By using the new approaches presented here  
693 (spectral filtering, microfluidics, rotating instrument) turbulent fluxes can be determined without  
694 contamination from current velocities, surface waves, or bias due to sensor separation. The spectral  
695 analysis framework can also be applied to standard eddy covariance and gradient exchange  
696 systems to reduce the bias created by wave-sensitive sensors and bias in turbulence and velocity  
697 measurements. The application of the presented spectral analysis framework requires  
698 measurements to be conducted at sufficient heights from the interface, and also has the significant  
699 benefit of allowing for chemical sensors with slower response times, enabling new sensor and  
700 tracer applications to the EC technique.

701

## 702 **Acknowledgments**

703 This work benefitted from numerous discussions with Malcolm Scully, John Trowbridge,  
704 Jennie Rheuban, Wade McGillis, and the wider aquatic EC community, in general. We thank  
705 Jennie Rheuban, Daniel McCorkle, Brian Hopkinson, and Kyle Conner for assistance with field  
706 work. This work was supported by the Independent Research & Development Program at WHOI  
707 and NSF OCE grants 1657727 and 1633951. The author declares no conflict of interest. Data for  
708 this study are archived at the Biological & Chemical Oceanography Data Management Office per  
709 NSF policies (<https://www.bco-dmo.org/person/560155>).

710 **References Cited**

- 711 Attard, K.M., Glud, R.N., McGinnis, D.F. and Rysgaard, S., 2014. Seasonal rates of benthic  
712 primary production in a Greenland fjord measured by aquatic eddy correlation. *Limnology and*  
713 *Oceanography*, 59(5), pp.1555-1569. doi:10.4319/lo.2014.59.5.1555
- 714 Attard, K.M., Stahl, H., Kamenos, N.A., Turner, G., Burdett, H.L. and Glud, R.N., 2015. Benthic  
715 oxygen exchange in a live coralline algal bed and an adjacent sandy habitat: an eddy covariance  
716 study. *Marine Ecology Progress Series*, 535, pp.99-115.
- 717 Attard, K.M., Hancke, K., Sejr, M.K. and Glud, R.N., 2016. Benthic primary production and  
718 mineralization in a High Arctic fjord: in situ assessments by aquatic eddy covariance. *Marine*  
719 *ecology progress series*, 554, pp.35-50.
- 720 Attard, K.M., Søgaard, D.H., Piontek, J., Lange, B.A., Katlein, C., Sørensen, H.L., McGinnis,  
721 D.F., Rovelli, L., Rysgaard, S., Wenzhöfer, F. and Glud, R.N., 2018. Oxygen fluxes beneath  
722 Arctic land-fast ice and pack ice: towards estimates of ice productivity. *Polar Biology*, 41(10),  
723 pp.2119-2134.
- 724 Attard, K.M., Rodil, I.F., Glud, R.N., Berg, P., Norkko, J. and Norkko, A., 2019. Seasonal  
725 ecosystem metabolism across shallow benthic habitats measured by aquatic eddy  
726 covariance. *Limnology and oceanography letters*, 4(3), pp.79-86. doi: 10.1002/lol2.10107
- 727 Baldocchi DD (2003) Assessing the eddy covariance technique for evaluating carbon dioxide  
728 exchange rates of ecosystems: past, present and future. *Global Change Biology* 9: 479-492.  
729 DOI: 10.1046/j.1365-2486.2003.00629.x
- 730 Berg, P., H. Røy, F. Janssen, V. Meyer, B. Jørgensen, M. Huettel, and D. de Beer (2003),  
731 Oxygen uptake by aquatic sediments measured with a novel non-invasive eddy-correlation  
732 technique, *Mar. Ecol. Prog. Ser.*, 261, 75-83, doi:10.3354/meps261075.
- 733 Berg, P. and Huettel, M., 2008. Monitoring the seafloor using the noninvasive eddy correlation  
734 technique. *Oceanography*, 21(4), pp.164-167.
- 735 Berg, P., Glud, R.N., Hume, A., Stahl, H., Oguri, K., Meyer, V. and Kitazato, H., 2009. Eddy  
736 correlation measurements of oxygen uptake in deep ocean sediments. *Limnology and*  
737 *Oceanography: Methods*, 7(8), pp.576-584. doi.org/10.4319/lom.2009.7.576
- 738 Berg, P., Long, M.H., Huettel, M., Rheuban, J.E., McGlathery, K.J., Howarth, R.W., Foreman,  
739 K.H., Giblin, A.E. and Marino, R., 2013. Eddy correlation measurements of oxygen fluxes in  
740 permeable sediments exposed to varying current flow and light. *Limnology and*  
741 *Oceanography*, 58(4), pp.1329-1343.
- 742 Berg, P., C. E. Reimers, J. Rosman, T. Özkan-Haller, M. Huettel, M. L. Delgard. (2015).  
743 Technical Note: Time lag correction of aquatic eddy covariance data measured in the presence of  
744 waves. *Biogeosciences Discuss.* 12: 8395-8427. doi: 10.5194/bgd-12-8395-2015.
- 745 Berg, P., Koopmans, D.J., Huettel, M., Li, H., Mori, K. and Wüest, A., 2016. A new robust  
746 oxygen-temperature sensor for aquatic eddy covariance measurements. *Limnology and*  
747 *Oceanography: Methods*, 14(3), pp.151-167. doi.org/10.1002/lom3.10071
- 748 Berg, P. and Pace, M.L., 2017. Continuous measurement of air–water gas exchange by  
749 underwater eddy covariance. *Biogeosciences*, 14(23), pp.5595-5606. doi.org/10.5194/bg-14-  
750 5595-2017

- 751 Berg, P., Delgard, M.L., Polsenaere, P., McGlathery, K.J., Doney, S.C. and Berger, A.C., 2019.  
752 Dynamics of benthic metabolism, O<sub>2</sub>, and pCO<sub>2</sub> in a temperate seagrass meadow. *Limnology*  
753 *and Oceanography*, 64(6), pp.2586-2604.
- 754 Berger, A.C., Berg, P., McGlathery, K.J. and Delgard, M.L., 2020. Long-term trends and  
755 resilience of seagrass metabolism: A decadal aquatic eddy covariance study. *Limnology and*  
756 *Oceanography*.
- 757 Brand, A, McGinnis, D.F., Wehrli, B., Wuest, A. 2008. Intermittent oxygen flux from the  
758 interior into the bottom boundary of lakes as observed by eddy correlation. *Limnology and*  
759 *Oceanography*, 53(5), pp. 1997-2006.
- 760 Burba, G. and Anderson, D., (2010). A brief practical guide to eddy covariance flux  
761 measurements: principles and workflow examples for scientific and industrial applications. LI-  
762 COR Biosciences, Lincoln, Nebraska, USA, 212 pp.: <http://www.licor.com/eddycovariance>
- 763 Cathalot, C., Oevelen, D.V., Cox, T.J., Kutti, T., Lavaleye, M.S., Duineveld, G.C., & Meysman,  
764 F.J. (2015). Cold-water coral reefs and adjacent sponge grounds: hotspots of benthic respiration  
765 and organic carbon cycling in the deep sea. *Frontiers in Marine Science*, 2, 1-12.
- 766 Chipman, L., Huettel, M., Berg, P., Meyer, V., Klimant, I., Glud, R. and Wenzhoefer, F., 2012.  
767 Oxygen optodes as fast sensors for eddy correlation measurements in aquatic  
768 systems. *Limnology and Oceanography: Methods*, 10(5), pp.304-316.
- 769 Crusius, J., Berg, P., Koopmans, D.J. and Erban, L., 2008. Eddy correlation measurements of  
770 submarine groundwater discharge. *Marine Chemistry*, 109(1-2), pp.77-85.
- 771 Cyronak, T., Santos, I.R., McMahon, A. and Eyre, B.D., 2013. Carbon cycling hysteresis in  
772 permeable carbonate sands over a diel cycle: Implications for ocean acidification. *Limnology and*  
773 *Oceanography*, 58(1), pp.131-143. doi.org/10.4319/lo.2013.58.1.0131
- 774 de Froe, E., Rovelli, L., Glud, R.N., Maier, S.R., Duineveld, G., Mienis, F., Lavaleye, M. and  
775 van Oevelen, D., 2019. Benthic oxygen and nitrogen exchange on a cold-water coral reef in the  
776 North-East Atlantic Ocean. *Frontiers in Marine Science*, 6, p.665.
- 777 Donis, D., Holtappels, M., Noss, C., Cathalot, C., Hancke, K., Polsenaere, P., & McGinnis, D. F.  
778 (2015). An assessment of the precision and confidence of aquatic eddy correlation  
779 measurements. *Journal of Atmospheric and Oceanic Technology*, 32(3), 642-655.  
780 doi.org/10.1175/JTECH-D-14-00089.1
- 781 Donis, D., McGinnis, D.F., Holtappels, M., Felden, J. and Wenzhoefer, F., 2016. Assessing  
782 benthic oxygen fluxes in oligotrophic deep sea sediments (HAUSGARTEN observatory). *Deep*  
783 *Sea Research Part I: Oceanographic Research Papers*, 111, pp.1-10.
- 784 Duarte, C.M., Marbà, N., Gacia, E., Fourqurean, J.W., Beggins, J., Barrón, C. and Apostolaki,  
785 E.T., 2010. Seagrass community metabolism: Assessing the carbon sink capacity of seagrass  
786 meadows. *Global Biogeochemical Cycles*, 24(4). doi.org/10.1029/2010GB003793
- 787 Edson, J. B., Hinton, A. A., Prada, K. E., Hare, J. E., & Fairall, C. W. (1998). Direct covariance  
788 flux estimates from mobile platforms at sea. *Journal of Atmospheric and Oceanic*  
789 *Technology*, 15(2), 547-562. doi.org/10.1175/1520-0426(1998)015<0547:DCFEFM>2.0.CO;2

- 790 Edson, J.B., Zappa, C.J., Ware, J.A., McGillis, W.R. and Hare, J.E., 2004. Scalar flux profile  
791 relationships over the open ocean. *Journal of Geophysical Research: Oceans*, 109(C8).  
792 doi.org/10.1029/2003JC001960
- 793 Else, B.G.T., Rysgaard, S., Attard, K., Campbell, K., Crabeck, O., Galley, R.J., Geilfus, N.X.,  
794 Lemes, M., Lueck, R., Papakyriakou, T. and Wang, F., 2015. Under-ice eddy covariance flux  
795 measurements of heat, salt, momentum, and dissolved oxygen in an artificial sea ice pool. *Cold*  
796 *Regions Science and Technology*, 119, pp.158-169.
- 797 Fairaill, C.W., Hare, J.E., Edson, J.B. and McGillis, W., 2000. Parameterization and  
798 micrometeorological measurement of air-sea gas transfer. *Boundary-Layer Meteorology*, 96(1-  
799 2), pp.63-106.
- 800 Flügge, M., Paskyabi, M. B., Reuder, J., Edson, J. B., & Plueddemann, A. J. (2016). Comparison  
801 of Direct Covariance Flux Measurements from an Offshore Tower and a Buoy. *Journal of*  
802 *Atmospheric and Oceanic Technology*, 33(5), 873-890. doi.org/10.1175/JTECH-D-15-0109.1
- 803 Gerbi, G.P., Trowbridge, J.H., Edson, J.B., Plueddemann, A.J., Terray, E.A. and Fredericks, J.J.  
804 2008. Measurements of momentum and heat transfer across the air-sea interface. *Journal of*  
805 *Physical Oceanography*, 38(5), 1054-1072. doi.org/10.1175/2007JPO3739.1
- 806 Glud, R.N., Berg, P., Hume, A., Batty, P., Blicher, M.E., Lennert, K. and Rysgaard, S., 2010.  
807 Benthic O<sub>2</sub> exchange across hard-bottom substrates quantified by eddy correlation in a sub-  
808 Arctic fjord. *Marine ecology progress series*, 417, pp.1-12.
- 809 Glud, R.N., Rysgaard, S., Turner, G., McGinnis, D.F. and Leakey, R.J., 2014. Biological-and  
810 physical-induced oxygen dynamics in melting sea ice of the Fram Strait. *Limnology and*  
811 *oceanography*, 59(4), pp.1097-1111.
- 812 Glud, R.N., Berg, P., Stahl, H., Hume, A., Larsen, M., Eyre, B.D. and Cook, P.L., 2016. Benthic  
813 carbon mineralization and nutrient turnover in a Scottish sea loch: an integrative in situ  
814 study. *Aquatic Geochemistry*, 22(5-6), pp.443-467.
- 815 Holtappels, M. and Lorke, A., 2011. Estimating turbulent diffusion in a benthic boundary  
816 layer. *Limnology and Oceanography: Methods*, 9(1), pp.29-41.
- 817 Holtappels, M., Glud, R.N., Donis, D., Liu, B., Hume, A., Wenzhöfer, F. and Kuypers, M.M.,  
818 2013. Effects of transient bottom water currents and oxygen concentrations on benthic exchange  
819 rates as assessed by eddy correlation measurements. *Journal of Geophysical Research:*  
820 *Oceans*, 118(3), pp.1157-1169. doi.org/10.1002/jgrc.20112
- 821 Holtappels, M., Noss, C., Hancke, K., Cathalot, C., McGinnis, D. F., Lorke, A., & Glud, R. N.  
822 (2015). Aquatic Eddy Correlation: Quantifying the Artificial Flux Caused by Stirring-Sensitive  
823 O<sub>2</sub> Sensors. *PloS one*, 10(1), e0116564. doi.org/10.1371/journal.pone.0116564
- 824 Hopkinson BM, King AC, Johnson-Roberson M, Long MH, Bhandarkar M. (2020) Automated  
825 classification of three-dimensional reconstructions of coral reefs using convolutional neural  
826 networks. *PLoS ONE* 15(3): e0230671. DOI: 10.1371/journal.pone.0230671
- 827 Hume, A, P Berg, KJ McGlathery. (2011) Dissolved oxygen fluxes and ecosystem metabolism in  
828 an eelgrass (*Zostera marina*) meadow measured with the novel eddy correlation technique.  
829 *Limnol. Oceanogr.* 56: 86–96.

- 830 Johnson, K.S., Barry, J.P., Coletti, L.J., Fitzwater, S.E., Jannasch, H.W. and Lovera, C.F., 2011.  
831 Nitrate and oxygen flux across the sediment-water interface observed by eddy correlation  
832 measurements on the open continental shelf. *Limnology and Oceanography: Methods*, 9(11),  
833 pp.543-553.
- 834 Klimant, I., Meyer, V. and Köhl, M., 1995. Fiber-optic oxygen microsensors, a new tool in  
835 aquatic biology. *Limnology and Oceanography*, 40(6), pp.1159-1165.
- 836 Koopmans, D.J. and Berg, P., 2015. Stream oxygen flux and metabolism determined with the  
837 open water and aquatic eddy covariance techniques. *Limnology and Oceanography*, 60(4),  
838 pp.1344-1355.
- 839 Koopmans, D., Holtappels, M., Chennu, A., Weber, M. and de Beer, D., 2020. High Net Primary  
840 Production of Mediterranean Seagrass (*Posidonia oceanica*) Meadows Determined With Aquatic  
841 Eddy Covariance. *Frontiers in marine science*, 7: 118. doi: 10.3389/fmars.2020.00118
- 842 Kreling, J., Bravidor, J., McGinnis, D.F., Koschorreck, M. and Lorke, A., 2014. Physical  
843 controls of oxygen fluxes at pelagic and benthic oxyclines in a lake. *Limnology and*  
844 *Oceanography*, 59(5), pp.1637-1650. doi.org/10.4319/lo.2014.59.5.1637
- 845 Kuwae, T., Kamio, K., Inoue, T., Miyoshi, E. and Uchiyama, Y., 2006. Oxygen exchange flux  
846 between sediment and water in an intertidal sandflat, measured in situ by the eddy-correlation  
847 method. *Marine Ecology Progress Series*, 307, pp.59-68.
- 848 Lee, J.S., Kang, D.J., Hineva, E., Slabakova, V., Todorova, V., Park, J. and Cho, J.H., 2017.  
849 Estimation of net ecosystem metabolism of seagrass meadows in the coastal waters of the East  
850 Sea and Black Sea using the noninvasive eddy covariance technique. *Ocean Science*  
851 *Journal*, 52(2), pp.243-256.
- 852 Lee, X., W. Massman, and B. Law (Eds.).2004. "Handbook of Micrometeorology: A Guide for  
853 Surface Flux Measurement and Analysis". Springer-Verlag, 250 pp.
- 854 Long, M.H., Rheuban, J.E., Berg, P. and Ziemann, J.C., 2012b. A comparison and correction of  
855 light intensity loggers to photosynthetically active radiation sensors. *Limnology and*  
856 *Oceanography: Methods*, 10(6), pp.416-424.
- 857 Long, M.H., Koopmans, D., Berg, P., Rysgaard, S., Glud, R.N. and Søgaard, D.H., 2012a.  
858 Oxygen exchange and ice melt measured at the ice-water interface by eddy  
859 correlation. *Biogeosciences*, 9(6). doi:10.5194/bg-9-1957-2012
- 860 Long, M. H., P. Berg, D. de Beer, and J. C. Ziemann (2013), In situ coral reef oxygen metabolism:  
861 an eddy correlation study., PLoS One, 8(3), e58581, doi:10.1371/journal.pone.0058581.
- 862 Long, M.H., Charette, M.A., Martin, W.R. and McCorkle, D.C., 2015a. Oxygen metabolism and  
863 pH in coastal ecosystems: Eddy Covariance Hydrogen ion and Oxygen Exchange System  
864 (ECHOES). *Limnology and Oceanography: Methods*, 13(8), pp.438-450.  
865 doi:10.1002/lom3.10038.
- 866 Long, M. H., P. Berg, K. J. McGlathery, and J. C. Ziemann (2015b), Sub-tropical seagrass  
867 ecosystem metabolism measured by eddy covariance, Mar. Ecol. Prog. Ser., 529, 75–90,  
868 doi:10.3354/meps11314.

- 869 Long, M.H., Berg, P. and Falter, J.L., 2015c. Seagrass metabolism across a productivity gradient  
870 using the eddy covariance, Eulerian control volume, and biomass addition techniques. *Journal of*  
871 *Geophysical Research: Oceans*, 120(5), pp.3624-3639. doi.org/10.1002/2014JC010352
- 872 Long, M.H. and Nicholson, D.P., 2018. Surface gas exchange determined from an aquatic eddy  
873 covariance floating platform. *Limnology and Oceanography: Methods*, 16(3), pp.145-159.  
874 doi.org/10.1002/lom3.10233
- 875 Long, M.H., Rheuban, J.E., McCorkle, D.C., Burdige, D.J. and Zimmerman, R.C., 2019. Closing  
876 the oxygen mass balance in shallow coastal ecosystems. *Limnology and Oceanography*, 64(6),  
877 pp.2694-2708. doi.org/10.1002/lno.11248
- 878 Long, M.H., Sutherland, K., Wankel, S.D., Burdige, D.J. and Zimmerman, R.C., 2020. Ebullition  
879 of oxygen from seagrasses under supersaturated conditions. *Limnology and*  
880 *oceanography*, 65(2), pp.314-324. doi.org/10.1002/lno.11299
- 881 Lorke, A., McGinnis, D.F., Maeck, A. and Fischer, H., 2012. Effect of ship locking on sediment  
882 oxygen uptake in impounded rivers. *Water Resources Research*, 48(12).
- 883 Lorke, A., McGinnis, D.F. and Maeck, A., 2013. Eddy-correlation measurements of benthic  
884 fluxes under complex flow conditions: Effects of coordinate transformations and averaging time  
885 scales. *Limnology and Oceanography: Methods*, 11(8), pp.425-437.
- 886 Lorrai, C., McGinnis, D.F., Berg, P., Brand, A. and Wüest, A., 2010. Application of oxygen  
887 eddy correlation in aquatic systems. *Journal of Atmospheric and Oceanic Technology*, 27(9),  
888 pp.1533-1546.
- 889 Lumley, J.L. and Terray, E.A., 1983. Kinematics of turbulence convected by a random wave  
890 field. *Journal of Physical Oceanography*, 13(11), pp.2000-2007.
- 891 McCann-Grosvenor, K., Reimers, C.E. and Sanders, R.D., 2014. Dynamics of the benthic  
892 boundary layer and seafloor contributions to oxygen depletion on the Oregon inner  
893 shelf. *Continental Shelf Research*, 34, pp.93-106.
- 894 McGillis, W.R., Edson, J.B., Hare, J.E. and Fairall, C.W., 2001. Direct covariance air-sea CO<sub>2</sub>  
895 fluxes. *Journal of Geophysical Research: Oceans*, 106(C8), pp.16729-16745.  
896 doi.org/10.1029/2000JC000506
- 897 McGillis, W. R., C. Langdon, A. J. Williams, B. Loose, 2009. O<sub>2</sub> MAVS: an Instrument for  
898 Measuring Oxygen Flux, MTS/IEEE Biloxi - Marine Technology for Our Future: Global and  
899 Local Challenges, OCEANS 2009, No. 5422166.
- 900 McGillis, W. R., C. Langdon, B. Loose, K. K.Yates, J. Corredor, 2011. Productivity of a coral  
901 reef using boundary layer and enclosure methods, *Geophys. Res. Lett.*, 38, L L03611,  
902 doi:10.1029/2010GL046179.
- 903 McGinnis, D.F., Berg, P., Brand, A., Lorrai, C., Edmonds, T.J. and Wüest, A., 2008.  
904 Measurements of eddy correlation oxygen fluxes in shallow freshwaters: Towards routine  
905 applications and analysis. *Geophysical Research Letters*, 35(4).
- 906 McGinnis, D.F., Cherednichenko, S., Sommer, S., Berg, P., Rovelli, L., Schwarz, R., Glud, R.N.  
907 and Linke, P., 2011. Simple, robust eddy correlation amplifier for aquatic dissolved oxygen and  
908 hydrogen sulfide flux measurements. *Limnology and Oceanography: Methods*, 9(8), pp.340-347.

- 909 McGinnis, D.F., Sommer, S., Lorke, A., Glud, R.N. and Linke, P., 2014. Quantifying tidally  
910 driven benthic oxygen exchange across permeable sediments: An aquatic eddy correlation  
911 study. *Journal of Geophysical Research: Oceans*, 119(10), pp.6918-6932.
- 912 Muehllehner, N., Langdon, C., Venti, A. and Kadko, D., 2016. Dynamics of carbonate  
913 chemistry, production, and calcification of the Florida Reef Tract (2009–2010): Evidence for  
914 seasonal dissolution. *Global Biogeochemical Cycles*, 30(5), pp.661-688.  
915 doi.org/10.1002/2015GB005327
- 916 Murniati, E., Geissler, S. and Lorke, A., 2015. Short-term and seasonal variability of oxygen  
917 fluxes at the sediment–water interface in a riverine lake. *Aquatic Sciences*, 77(2), pp.183-196.
- 918 Nepf, H.M., 2012. Flow and transport in regions with aquatic vegetation. *Annu. Rev. Fluid Mech.*  
919 *2012*. 44:123–42. doi: 10.1146/annurev-fluid-120710-101048
- 920 Owen DP, Long MH, Fitt WK, Hopkinson BM. Taxon-specific primary production rates on  
921 coral reefs in the Florida Keys. *Limnology and Oceanography*. LO-20-0165
- 922 Plew, D.R., 2019. Investigating benthic impacts at salmon farms using eddy covariance  
923 measurements of benthic oxygen fluxes. *Aquaculture Environment Interactions*, 11, pp.337-357.
- 924 Reidenbach, M.A., Berg, P., Hume, A., Hansen, J.C. and Whitman, E.R., 2013. Hydrodynamics  
925 of intertidal oyster reefs: The influence of boundary layer flow processes on sediment and  
926 oxygen exchange. *Limnology and Oceanography: Fluids and Environments*, 3(1), pp.225-239.
- 927 Reimers, C.E., Özkan-Haller, H., Berg, P., Devol, A., McCann-Grosvenor, K. and Sanders, R.D.,  
928 2012. Benthic oxygen consumption rates during hypoxic conditions on the Oregon continental  
929 shelf: Evaluation of the eddy correlation method. *Journal of Geophysical Research:*  
930 *Oceans*, 117(C2).
- 931 Reimers, C. E., Özkan-Haller, H. T., Albright, A. T., & Berg, P. (2016a). Microelectrode  
932 velocity effects and aquatic eddy covariance measurements under waves. *Journal of Atmospheric*  
933 *and Oceanic Technology*, 33(2), 263-282.
- 934 Reimers, C.E., Özkan-Haller, H.T., Sanders, R.D., McCann-Grosvenor, K., Chace, P.J. and  
935 Crowe, S.A., 2016b. The dynamics of benthic respiration at a mid-shelf station off  
936 Oregon. *Aquatic geochemistry*, 22(5-6), pp.505-527.
- 937 Revsbech, N.P., 1989. An oxygen microsensor with a guard cathode. *Limnology and*  
938 *Oceanography*, 34(2), pp.474-478.
- 939 Rheuban JE and P Berg (2013) The effects of spatial and temporal variability at the sediment  
940 surface on aquatic eddy correlation flux measurements. *Limnol Oceanogr Meth* 11: 351-359.
- 941 Rheuban, J.E., Berg, P. and McGlathery, K.J., 2014a. Multiple timescale processes drive  
942 ecosystem metabolism in eelgrass (*Zostera marina*) meadows. *Marine Ecology Progress*  
943 *Series*, 507, pp.1-13.
- 944 Rheuban, J.E., Berg, P. and McGlathery, K.J., 2014b. Ecosystem metabolism along a  
945 colonization gradient of eelgrass (*Zostera marina*) measured by eddy correlation. *Limnology and*  
946 *oceanography*, 59(4), pp.1376-1387.

- 947 Rodil, I.F., Attard, K.M., Norkko, J., Glud, R.N. and Norkko, A., 2019. Towards a sampling  
948 design for characterizing habitat-specific benthic biodiversity related to oxygen flux dynamics  
949 using Aquatic Eddy Covariance. *PloS one*, 14(2).
- 950 Rovelli, L., Attard, K.M., Bryant, L.D., Flögel, S., Stahl, H., Roberts, J.M., Linke, P. and Glud,  
951 R.N., 2015. Benthic O<sub>2</sub> uptake of two cold-water coral communities estimated with the non-  
952 invasive eddy correlation technique. *Marine Ecology Progress Series*, 525, pp.97-104.
- 953 Rovelli, L., Attard, K.M., Binley, A., Heppell, C.M., Stahl, H., Trimmer, M. and Glud, R.N.,  
954 2017. Reach-scale river metabolism across contrasting sub-catchment geologies: Effect of light  
955 and hydrology. *Limnology and oceanography*, 62(S1), pp.S381-S399.
- 956 Rovelli, L., Attard, K.M., Heppell, C.M., Binley, A., Trimmer, M. and Glud, R.N., 2018.  
957 Headwater gas exchange quantified from O<sub>2</sub> mass balances at the reach scale. *Limnology and*  
958 *Oceanography: Methods*, 16(10), pp.696-709.
- 959 Rovelli, L., Attard, K.M., Cárdenas, C.A. and Glud, R.N., 2019. Benthic primary production and  
960 respiration of shallow rocky habitats: a case study from South Bay (Doumer Island, Western  
961 Antarctic Peninsula). *Polar biology*, 42(8), pp.1459-1474.
- 962 Santos, I.R., Glud, R.N., Maher, D., Erler, D. and Eyre, B.D., 2011. Diel coral reef acidification  
963 driven by porewater advection in permeable carbonate sands, Heron Island, Great Barrier  
964 Reef. *Geophysical Research Letters*, 38(3). doi:10.1029/2010GL046053
- 965 Scully, M.E., Trowbridge, J.H. and Fisher, A.W., 2016. Observations of the transfer of energy  
966 and momentum to the oceanic surface boundary layer beneath breaking waves. *Journal of*  
967 *Physical Oceanography*, 46(6), pp.1823-1837. doi.org/10.1175/JPO-D-15-0165.1
- 968 Shaw, W.J. and Trowbridge, J.H., 2001. The direct estimation of near-bottom turbulent fluxes in  
969 the presence of energetic wave motions. *Journal of Atmospheric and Oceanic Technology*, 18(9),  
970 pp.1540-1557.
- 971 Swinbank, W.C., 1951. The measurement of vertical transfer of heat and water vapor by eddies  
972 in the lower atmosphere. *Journal of Meteorology*, 8(3), pp.135-145.
- 973 Takeshita, Y., W.R. McGillis, E.M. Briggs, A.L. Carter, E.M. Donham, T.R. Martz (2016).  
974 Assessment of net community production and calcification of a coral reef using a boundary layer  
975 approach. *Journal of Geophysical Research: Oceans*, 121 (8), 5655-5671.
- 976 Trowbridge, J.H., 1998. On a technique for measurement of turbulent shear stress in the presence  
977 of surface waves. *Journal of Atmospheric and Oceanic Technology*, 15(1), pp.290-298.
- 978 Trowbridge, J.H. and Lentz, S.J., 2018. The bottom boundary layer. *Annual review of marine*  
979 *science*, 10, pp.397-420.
- 980 Trowbridge, J., Scully, M. and Sherwood, C.R., 2018. The cospectrum of stress-carrying  
981 turbulence in the presence of surface gravity waves. *Journal of Physical Oceanography*, 48(1),  
982 pp.29-44. doi.org/10.1175/JPO-D-17-0016.1
- 983 Turk, D., J.M. Bedard, W.J. Burt, S. Vagle, H. Thomas, K. Azetsu-Scott, W. R. McGillis (2016)  
984 Inorganic carbon in a high latitude estuary-fjord system in Canada's eastern Arctic. *Estuarine,*  
985 *Coastal and Shelf Science*, 178, 137-147.

- 986 Volaric, M.P., Berg, P. and Reidenbach, M.A., 2018. Oxygen metabolism of intertidal oyster  
987 reefs measured by aquatic eddy covariance. *Marine Ecology Progress Series*, 599, pp.75-91.
- 988 Volaric, M.P., Berg, P. and Reidenbach, M.A., 2019. An invasive macroalga alters ecosystem  
989 metabolism and hydrodynamics on a tidal flat. *Marine Ecology Progress Series*, 628, pp.1-16.
- 990 Volaric, M.P., Berg, P. and Reidenbach, M.A., 2020. Drivers of Oyster Reef Ecosystem  
991 Metabolism Measured Across Multiple Timescales. *Estuaries and Coasts*, pp.1-12.
- 992 Weck, J. and Lorke, A., 2017. Mixing efficiency in the thermocline of lakes observed from eddy  
993 correlation flux measurements. *Journal of Geophysical Research: Oceans*, 122(1), pp.291-305.  
994 doi.org/10.1002/2016JC012188
- 995 Wyngaard, J.C. and Coté, O.R., 1972. Cospectral similarity in the atmospheric surface  
996 layer. *Quarterly Journal of the Royal Meteorological Society*, 98(417), pp.590-603.
- 997 Yamamoto, S., Kayanne, H., Tokoro, T., Kuwae, T. and Watanabe, A., 2015. Total alkalinity  
998 flux in coral reefs estimated from eddy covariance and sediment pore-water profiles. *Limnology  
999 and Oceanography*, 60(1), pp.229-241.
- 1000 Zappa, C. J., P. A. Raymond, E. A. Terray, and W. R. McGillis, 2003. Variation in surface  
1001 turbulence and the gas transfer velocity over a tidal cycle in a macro-tidal estuary, *Estuaries*,  
1002 Vol. 26, No. 6, 1401-1415.